# A direct Eulerian GRP scheme for spherically symmetric general relativistic hydrodynamics

Kailiang Wu, Huazhong Tang [1]

*HEDPS, CAPT & LMAM, School of Mathematical Sciences, Peking University, Beijing 100871, P.R. China*

**Abstract**

The paper proposes a second-order accurate direct Eulerian generalized Riemann problem (GRP) scheme for the spherically symmetric general relativistic hydrodynamical (RHD) equations and a second-order accurate discretization for the spherically symmetric Einstein (SSE) equations. The former is directly using the Riemann invariants and the Runkine-Hugoniot jump conditions to analytically resolve the left and right nonlinear waves of the local GRP in the Eulerian formulation together with the local change of the metrics to obtain the limiting values of the time derivatives of the conservative variables along the cell interface and the numerical flux for the GRP scheme. While the latter utilizes the energy-momentum tensor obtained in the GRP solver to evaluate the fluid variables in the SSE equations and keeps the continuity of the metrics at the cell interfaces. Several numerical experiments show that the GRP scheme can achieve second-order accuracy and high resolution, and is effective for spherically symmetric general RHD problems.

*Key words:* Spherically symmetric general relativistic hydrodynamics; Godunov-type scheme; generalized Riemann problem; Riemann problem; Riemann invariant; Rankine-Hugoniot jump condition.

*Email addresses:* wukl@pku.edu.cn (Kailiang Wu), hztang@math.pku.edu.cn (Huazhong Tang).

[1] Corresponding author. Tel: +86-10-62757018; Fax: +86-10-62751801.

## 1 Introduction

Many fields such as high-energy astrophysics etc. may involve flows at speeds close to the speed of light or influenced by large gravitational potentials such that the relativistic effect should be taken into account. Relativistic flows appear in numerous astrophysical phenomena, from stellar to galactic scales, e.g. super-luminal jets, gamma-ray bursts, core collapse super-novae, coalescing neutron stars, formation of black holes and so on.

The governing equations of the relativistic hydrodynamics (RHD) are highly nonlinear so that their analytical treatment is extremely difficult. A primary and powerful approach to understand the physical mechanisms in RHDs is numerical simulations. The pioneering numerical work may date back to the finite difference code by May and White with the artificial viscosity technique for spherically symmetric general RHD equations in the Lagrangian coordinate [20,21]. Wilson first attempted to numerically solve multi-dimensional RHD equations in the Eulerian coordinate by using the finite difference method with the artificial viscosity technique [33], which was systematically introduced in [34]. Since 1990s, the numerical study of the RHDs began to attract considerable attention, and various modern shock-capturing methods based on exact or approximate Riemann solvers have been developed for the RHD equations, the readers are referred to the early review articles [19,5] and more recent works on numerical methods for the RHD equations in [35,36]. Recently, second-order accurate direct Eulerian generalized Riemann problem (GRP) schemes were developed for both 1D and 2D special RHD equations [40,41] and the third-order accurate extension to the 1D case was also presented in [38].

The GRP scheme, as an analytic high-order accurate extension of the Godunov method, was originally devised for non-relativistic compressible fluid dynamics [1], by utilizing a piecewise linear function to approximate the "initial" data and then analytically resolving a local GRP at each interface to yield numerical flux, see the comprehensive description in [2]. There exist two versions of the original GRP scheme: the Lagrangian and Eulerian. The Eulerian version is always derived by using the Lagrangian framework with a transformation, which is quite delicate, particularly for the sonic case and multi-dimensional application. To avoid those difficulties, second-order accurate direct Eulerian GRP schemes were respectively developed for the shallow water equations [12], the Euler equations [4], and a more general weakly coupled system [3] by directly resolving the local GRPs in the Eulerian formulation via the Riemann invariants and Rankine-Hugoniot jump conditions. A recent comparison of the GRP scheme with the gas-kinetic scheme showed the good performance of the GRP solver for some inviscid flow simulations [13]. Combined with the moving mesh method [29], the adaptive direct Eulerian GRP scheme was developed

in [9] with improved resolution as well as accuracy. The accuracy and performance of the adaptive GRP scheme were further studied in [10] in simulating 2D complex wave configurations formulated with the 2D Riemann problems of non-relativistic Euler equations. Recently, the adaptive GRP scheme was also extended to unstructured triangular meshes [16]. The third-order accurate extensions of the direct Eulerian GRP scheme were studied for 1D and 2D non-relativistic Euler equations in [37] and the general 1D hyperbolic balance laws in [25].

The aim of the paper is to develop a second-order accurate direct Eulerian GRP scheme for spherically symmetric general RHD equations. The traditional Godunov-type schemes based on exact or approximate Riemann solvers can be extended to the general RHD equations from the special RHD case through a local change of coordinates in terms of that the spacetime metric is locally Minkowskian [24]. Similar idea can be found in developing the so-called locally inertial Godunov method for spherically symmetric general RHD equations [32]. However, such approach cannot be used to develop the direct Eulerian GRP scheme for the general RHD equations, because it is necessary to resolve the local GRP together with the local change of the metrics taken into account. Moreover, the metrics should be approximately obtained at the cell interface by accurate scheme for the SSE equations to keep the continuity of the approximate metric functions. In short, developing the GRP scheme for the general RHD equations is not trivial and much more technical than the special relativistic case.

The paper is organized as follows. Section 2 introduces the governing equations of general RHDs in spherically symmetric spacetime and corresponding Riemann invariants as well as their total differentials. The second-order accurate direct Eulerian GRP scheme is developed in Section 3. The outline of the scheme is first given in Section 3.1. Then the local GRPs are analytically resolved in Section 3.2, where Sections 3.2.1 and 3.2.2 resolve the rarefaction and shock waves by using the Riemann invariants and the Rankine-Hugoniot jump conditions, respectively, Section 3.2.3 concludes the the limiting values of the time derivatives of the conservative variables at the "initial" discontinuous point along the cell interface for both nonsonic and sonic cases, and Section 3.2.4 discusses the acoustic case. Several numerical experiments are conducted in Section 4 to demonstrate the performance and accuracy of the proposed GRP scheme. Section 5 concludes the paper with several remarks.

## 2 Governing equations

The general RHD equations [5] consist of the local conservation laws of the current density $J^\mu$ and the stress-energy tensor $T^{\mu\nu}$

$$\nabla_\mu J^\mu = 0, \tag{2.1}$$
$$\nabla_\mu T^{\mu\nu} = 0, \tag{2.2}$$

where the indexes $\mu$ and $\nu$ run from 0 to 3, and $\nabla_\mu$ stands for the covariant derivative associated with the four-dimensional spacetime metric $g_{\mu\nu}$, that is, the proper spacetime distance between any two points in the four-dimensional spacetime can be measured by the line element $ds^2 = g_{\mu\nu}dx^\mu dx^\nu$. The current density is given by $J^\mu = \rho_0 u^\mu$, where $u^\mu$ represents the fluid four-velocity and $\rho_0$ denotes the proper rest-mass density. The stress-energy tensor for an ideal fluid is defined by

$$T^{\mu\nu} = (\rho + p)u^\mu u^\nu + pg^{\mu\nu},$$

in which $\rho$ and $p$ denote the rest energy density (including rest-mass) in the fluid frame and the pressure, respectively, and $g^{\mu\lambda}g_{\lambda\nu} = \delta^\mu_\nu$ with $\delta^\mu_\nu$ denoting the Kronecker symbol. The rest energy density $\rho$ can be expressed in terms of the rest-mass density $\rho_0$ and the internal energy $e$ as $\rho = \rho_0(c^2 + e)$, where $c$ denotes the speed of light in vacuum.

An additional equation for the thermodynamical variables, i.e. the so-called equation of state, is needed to close the system (2.1)–(2.2) for a fixed spacetime. This paper focuses on the equation of state describing barotropic fluids

$$p = p(\rho), \tag{2.3}$$

where $p(\rho)$ is a function of $\rho$ and satisfies

$$0 < \frac{dp}{d\rho} = p'(\rho) < 1. \tag{2.4}$$

It is worth noting that the equations (2.2)–(2.5) form a close system if $g^{\mu\nu}$ is given. In the general theory, the Einstein gravitational field equations relate the curvature of spacetime to the distribution of mass-energy in the following form

$$R^{\mu\nu} - \frac{1}{2}g^{\mu\nu}R = \kappa T^{\mu\nu}, \tag{2.5}$$

where $\kappa = \frac{8\pi\mathcal{G}}{c^4}$ is Einstein coupling constant, $\mathcal{G}$ is Newton's gravitational constant, and $R^{\mu\nu}$ and $R$ denote the Ricci tensor and the scalar curvature, respectively. For the sake of

convenience, units in which the speed of light $c$ and Newton's gravitational constant $\mathcal{G}$ are equal to one will be used throughout the paper.

The general RHD system in spherically symmetric spacetime is a simple but good "approximate" model in investigating several astrophysical phenomena, e.g. gamma-ray bursts, spherical accretion onto compact objects, and stellar collapse, etc. Its numerical methods have also received lots of attentions, see e.g. [20,6,27,39,17,18,22,26,8,32,23]. The spherically symmetric gravitational metrics in standard Schwarzschild coordinates are given by the line element [32]

$$ds^2 = -B(t,r)dt^2 + \frac{1}{A(t,r)}dr^2 + r^2(d\theta^2 + \sin^2\theta d\phi^2). \tag{2.6}$$

where $B(t,r)$ is called the *lapse function*, $(t,r)$ are temporal and radial coordinates, and $\boldsymbol{x} = (x^0, x^1, x^2, x^3) = (t, r, \theta, \phi)$ is the spacetime coordinate system. This paper is only concerned with the numerical method for the system (2.2)–(2.5) in spherically symmetric spacetime (2.6). Assume that the spherically symmetric metrics are Lipschitz and the stress-energy tensor is bounded in sup-norm, then the system (2.2)–(2.5) is weakly equivalent to the following system [7]

$$\frac{\partial \boldsymbol{U}}{\partial t} + \frac{\partial\left(\sqrt{AB}\boldsymbol{F}(\boldsymbol{U})\right)}{\partial r} = \boldsymbol{S}(r, A, B, \boldsymbol{U}), \tag{2.7}$$

$$\frac{\partial M}{\partial r} = \frac{1}{2}\kappa r^2 \mathcal{T}^{00}, \tag{2.8}$$

$$\frac{1}{B}\frac{\partial B}{\partial r} = \frac{1-A}{Ar} + \frac{\kappa r}{A}\mathcal{T}^{11}, \tag{2.9}$$

where

$$\boldsymbol{U} = (\mathcal{T}^{00}, \mathcal{T}^{01})^{\mathrm{T}}, \quad \boldsymbol{F} = (\mathcal{T}^{01}, \mathcal{T}^{11})^{\mathrm{T}},$$
$$\boldsymbol{S} = -\sqrt{AB}\left(\frac{2}{r}\mathcal{T}^{01}, \frac{2}{r}\mathcal{T}^{11} + \frac{1-A}{2Ar}(\mathcal{T}^{00} - \mathcal{T}^{11}) + \frac{\kappa r}{A}\left(\mathcal{T}^{00}\mathcal{T}^{11} - (\mathcal{T}^{01})^2\right) - \frac{2p}{r}\right)^{\mathrm{T}},$$

and the mass function $M$ is related to $A$ by $A = 1 - 2M/r$. Here

$$\mathcal{T}^{00} = (\rho + p)\, W^2 - p, \quad \mathcal{T}^{01} = (\rho + p)\, W^2 v, \quad \mathcal{T}^{11} = \left(\rho v^2 + p\right) W^2,$$

are the stress-energy tensor in locally flat Minkowski spacetime, related to $T^{\mu\nu}$ by

$$\mathcal{T}^{00} = BT^{00}, \quad \mathcal{T}^{01} = \sqrt{\frac{B}{A}}T^{01}, \quad \mathcal{T}^{11} = \frac{1}{A}T^{11},$$

and $W = 1/\sqrt{1-v^2}$ is the Lorentz factor with the velocity

$$v := \frac{1}{\sqrt{AB}}\frac{u^1}{u^0}.$$

Eq. (2.8) may be replaced with

$$\frac{\partial M}{\partial t} = -\frac{1}{2}\kappa r^2\sqrt{AB}\mathcal{T}^{01}, \tag{2.10}$$

to derive another equivalent system (2.7), (2.9), and (2.10).

The eigenvalues of the Jacobian matrix $\partial(\sqrt{AB}\boldsymbol{F})/\partial\boldsymbol{U}$ of (2.7) with (2.3) are

$$\lambda_- = \sqrt{AB}\left(\frac{v-c_s}{1-vc_s}\right), \quad \lambda_+ = \sqrt{AB}\left(\frac{v+c_s}{1+vc_s}\right),$$

where $c_s = \sqrt{p'(\rho)}$ denotes the local sound speed. Corresponding right eigenvectors $\boldsymbol{R}_\pm$, may be given as follows

$$\boldsymbol{R}_- = \begin{pmatrix} 1-vc_s \\ v-c_s \end{pmatrix}, \quad \boldsymbol{R}_+ = \begin{pmatrix} 1+vc_s \\ v+c_s \end{pmatrix},$$

and the inverse of the matrix $\boldsymbol{R} := (\boldsymbol{R}_-, \boldsymbol{R}_+)$ is

$$\boldsymbol{R}^{-1} = \frac{W^2}{2c_s}\begin{pmatrix} v+c_s & -(1+vc_s) \\ c_s-v & 1-vc_s \end{pmatrix}.$$

The condition (2.4) implies that $\lambda_- < \lambda_+$. Thus the system (2.7) is strictly hyperbolic. Moreover, both characteristic fields related to $\lambda_\pm$ are genuinely nonlinear if and only if the function $p(\rho)$ further satisfies [7]

$$p''(\rho) > -\frac{2p'(\rho)(1-p'(\rho))}{\rho+p(\rho)}, \tag{2.11}$$

which does always hold for

$$p(\rho) = \sigma^2\rho, \quad \sigma \in (0,1). \tag{2.12}$$

The Riemann invariants $\psi_\pm$ associated with the characteristic field $\lambda_\pm$ can be obtained as follows [7]

$$\psi_\pm = \frac{1}{2}\ln\left(\frac{1+v}{1-v}\right) \mp \int^\rho \frac{\sqrt{p'(\omega)}}{\omega+p(\omega)}d\omega, \tag{2.13}$$

which will play a pivotal role in resolving the centered rarefaction waves in the direct Eulerian GRP scheme for the RHD equations (2.7).

In the smooth region, by using (2.8) and (2.9), the RHD equations (2.7) can be reformed in the primitive variable vector $\boldsymbol{V} := (\rho, v)^{\mathrm{T}}$ as follows

$$\frac{\partial \boldsymbol{V}}{\partial t} + \boldsymbol{J}\frac{\partial \boldsymbol{V}}{\partial r} = \boldsymbol{H}, \tag{2.14}$$

where

$$\boldsymbol{J} = \frac{\sqrt{AB}}{1-v^2c_s^2}\begin{pmatrix} v(1-c_s^2) & \rho+p \\ \frac{(1-v^2)^2c_s^2}{\rho+p} & v(1-c_s^2) \end{pmatrix},$$

$$\boldsymbol{H} = (H_1, H_2)^{\mathrm{T}} = -\frac{\sqrt{AB}}{r(1-v^2c_s^2)}\begin{pmatrix} 2v(\rho+p)\left(1-\frac{\kappa r^2(\rho+p)}{4A}\right) \\ (1-v^2)\left(-2v^2c_s^2 + \frac{(1-A)(1-v^2c_s^2)}{2A} + \frac{\kappa r^2(p+\rho v^2c_s^2)}{2A}\right) \end{pmatrix}.$$

By using (2.14), one can derive the following differential relations of the Riemann invariants

$$\frac{D_\pm \psi_\mp}{Dt} = \frac{1}{1-v^2}\frac{D_\pm v}{Dt} \pm \frac{c_s}{\rho+p}\frac{D_\pm \rho}{Dt} = \frac{1}{1-v^2}H_2 \pm \frac{c_s}{\rho+p}H_1 =: s_\mp, \tag{2.15}$$

where

$$\frac{D_\pm}{Dt} := \frac{\partial}{\partial t} + \lambda_\pm \frac{\partial}{\partial r},$$

denote the total derivative operators along the characteristic curves $\frac{dr}{dt} = \lambda_\pm$.

## 3 Numerical scheme

### *3.1 The outline of the GRP scheme*

This subsection gives the outline of the GRP scheme. For the sake of simplicity, the equally spaced grid points $\left\{r_{j+\frac{1}{2}} = \left(j+\frac{1}{2}\right)\Delta r\right\}$ are used for the spatial domain $\Omega$ and the cell is denoted by $I_j = [r_{j-\frac{1}{2}}, r_{j+\frac{1}{2}}]$, $j \in \mathbb{Z}^+$. The time domain $[0, T]$ is also divided into the (non-uniform) grid $\{t_0 = 0, t_{n+1} = t_n + \Delta t_n, n \geq 0\}$ with the time step size $\Delta t_n$ determined by

$$\Delta t_n = C_{cfl}\frac{\Delta r}{\max\limits_j \left\{|\lambda_-(\boldsymbol{U}_j^n, A_j^n, B_j^n)|, |\lambda_+(\boldsymbol{U}_j^n, A_j^n, B_j^n)|\right\}},$$

where $\boldsymbol{U}_j^n$, $A_j^n$, and $B_j^n$ approximate the values of $\boldsymbol{U}(t,r)$, $A(t,r)$ and $B(t,r)$ at the point $(t_n, r_j)$, respectively, and $C_{cfl}$ is the CFL number.

Assume that the "initial" data at time $t = t_n$ are piecewise linear functions as follows

$$\begin{cases} \boldsymbol{U}_h(t_n, r) = \boldsymbol{U}_j^n + \boldsymbol{\sigma}_j^n (r - r_j) =: \boldsymbol{U}_j^n(r), \\ \begin{pmatrix} A_h(t_n, r) \\ B_h(t_n, r) \end{pmatrix} = \dfrac{r_{j+\frac{1}{2}} - r}{\Delta r} \begin{pmatrix} A_{j-\frac{1}{2}}^n \\ B_{j-\frac{1}{2}}^n \end{pmatrix} + \dfrac{r - r_{j-\frac{1}{2}}}{\Delta r} \begin{pmatrix} A_{j+\frac{1}{2}}^n \\ B_{j+\frac{1}{2}}^n \end{pmatrix}, \end{cases} \tag{3.1}$$

for $r \in I_j$, where $A_h(t_n, r)$ and $B_h(t_n, r)$ are continuous at cell interfaces $r_{j\pm\frac{1}{2}}$.

`Step I`. Evaluate the point values $\boldsymbol{U}_{j+\frac{1}{2}}^{n+\frac{1}{2}}$ approximating $\boldsymbol{U}(t_{n+\frac{1}{2}}, r_{j+\frac{1}{2}})$ by

$$\boldsymbol{U}_{j+\frac{1}{2}}^{n+\frac{1}{2}} = \boldsymbol{U}_{j+\frac{1}{2}}^{\mathrm{RP},n} + \frac{\Delta t_n}{2} \left( \frac{\partial \boldsymbol{U}}{\partial t} \right)_{j+\frac{1}{2}}^{\mathrm{GRP},n}, \tag{3.2}$$

where $\boldsymbol{U}_{j+\frac{1}{2}}^{\mathrm{RP},n}$ is the values at $r = r_{j+\frac{1}{2}}$ of the solutions to the following Riemann problem of the homogeneous hyperbolic conservation laws

$$\begin{cases} \dfrac{\partial \boldsymbol{U}}{\partial t} + \sqrt{A_{j+\frac{1}{2}}^n B_{j+\frac{1}{2}}^n} \dfrac{\partial \boldsymbol{F}(\boldsymbol{U})}{\partial r} = 0, \qquad r > 0,\ t > t_n, \\ \boldsymbol{U}(t_n, r) = \begin{cases} \boldsymbol{U}_{j+\frac{1}{2},L}^n := \boldsymbol{U}_h(t_n, r_{j+\frac{1}{2}} - 0), & r < r_{j+\frac{1}{2}}, \\ \boldsymbol{U}_{j+\frac{1}{2},R}^n := \boldsymbol{U}_h(t_n, r_{j+\frac{1}{2}} + 0), & r > r_{j+\frac{1}{2}}, \end{cases} \end{cases}$$

and $(\partial \boldsymbol{U}/\partial t)_{j+\frac{1}{2}}^{\mathrm{GRP},n}$ is analytically derived by a second order accurate resolution of the local generalized Riemann problem (GRP) at each point $(t_n, r_{j+\frac{1}{2}})$, i.e.

$$\begin{cases} \text{Eqs. (2.7)}, \qquad r > 0,\ t > t_n, \\ \boldsymbol{U}(t_n, r) = \begin{cases} \boldsymbol{U}_j^n(r), & r < r_{j+\frac{1}{2}}, \\ \boldsymbol{U}_{j+1}^n(r), & r > r_{j+\frac{1}{2}}. \end{cases} \end{cases} \tag{3.3}$$

The calculation of $(\partial \boldsymbol{U}/\partial t)_{j+\frac{1}{2}}^{\mathrm{GRP},n}$ is one of the key elements in the GRP scheme and will be given in Section 3.2.

`Step II`. Calculate the point values $A_{j+\frac{1}{2}}^{n+\frac{1}{2}}$ and $B_{j+\frac{1}{2}}^{n+\frac{1}{2}}$, which are approximation of $A(t_{n+\frac{1}{2}}, r_{j+\frac{1}{2}})$ and $B(t_{n+\frac{1}{2}}, r_{j+\frac{1}{2}})$, respectively, by

$$M_{j+\frac{1}{2}}^{n+\frac{1}{2}} = M_{j+\frac{1}{2}}^n + \frac{\Delta t_n}{2} \left( \frac{\partial M}{\partial t} \right)_{j+\frac{1}{2}}^n = M_{j+\frac{1}{2}}^n - \frac{\Delta t_n}{4} \kappa r_{j+\frac{1}{2}}^2 \sqrt{A_{j+\frac{1}{2}}^n B_{j+\frac{1}{2}}^n} \mathcal{T}^{01} \left( \boldsymbol{U}_{j+\frac{1}{2}}^{\mathrm{RP},n} \right),$$

$$A_{j+\frac{1}{2}}^{n+\frac{1}{2}} = 1 - 2M_{j+\frac{1}{2}}^{n+\frac{1}{2}} / r_{j+\frac{1}{2}},$$

$$\ln B_{j+\frac{1}{2}}^{n+\frac{1}{2}} = \ln B_{j-\frac{1}{2}}^{n+\frac{1}{2}} + \frac{\Delta r}{2}\left(\frac{1-A_{j-\frac{1}{2}}^{n+\frac{1}{2}}}{A_{j-\frac{1}{2}}^{n+\frac{1}{2}} r_{j-\frac{1}{2}}} + \frac{\kappa r_{j-\frac{1}{2}}}{A_{j-\frac{1}{2}}^{n+\frac{1}{2}}}\mathcal{T}^{11}\left(\boldsymbol{U}_{j-\frac{1}{2}}^{n+\frac{1}{2}}\right) + \frac{1-A_{j+\frac{1}{2}}^{n+\frac{1}{2}}}{A_{j+\frac{1}{2}}^{n+\frac{1}{2}} r_{j+\frac{1}{2}}} + \frac{\kappa r_{j+\frac{1}{2}}}{A_{j+\frac{1}{2}}^{n+\frac{1}{2}}}\mathcal{T}^{11}\left(\boldsymbol{U}_{j+\frac{1}{2}}^{n+\frac{1}{2}}\right)\right).$$

`Step III`. Approximately evolve the solution vector $\boldsymbol{U}$ at time $t_{n+1}$ of (2.7) by a second-order accurate Godunov-type scheme

$$\begin{aligned}\boldsymbol{U}_j^{n+1} =& \boldsymbol{U}_j^n - \frac{\Delta t_n}{\Delta r}\left(\sqrt{A_{j+\frac{1}{2}}^{n+\frac{1}{2}} B_{j+\frac{1}{2}}^{n+\frac{1}{2}}}\boldsymbol{F}\left(\boldsymbol{U}_{j+\frac{1}{2}}^{n+\frac{1}{2}}\right) - \sqrt{A_{j-\frac{1}{2}}^{n+\frac{1}{2}} B_{j-\frac{1}{2}}^{n+\frac{1}{2}}}\boldsymbol{F}\left(\boldsymbol{U}_{j-\frac{1}{2}}^{n+\frac{1}{2}}\right)\right)\\ &+ \frac{\Delta t_n}{2}\left(\boldsymbol{S}\left(r_{j-\frac{1}{2}}, A_{j-\frac{1}{2}}^{n+\frac{1}{2}}, B_{j-\frac{1}{2}}^{n+\frac{1}{2}}, \boldsymbol{U}_{j-\frac{1}{2}}^{n+\frac{1}{2}}\right) + \boldsymbol{S}\left(r_{j+\frac{1}{2}}, A_{j+\frac{1}{2}}^{n+\frac{1}{2}}, B_{j+\frac{1}{2}}^{n+\frac{1}{2}}, \boldsymbol{U}_{j+\frac{1}{2}}^{n+\frac{1}{2}}\right)\right). \end{aligned} \tag{3.4}$$

`Step V`. Calculate $A_{j+\frac{1}{2}}^{n+1}$ and $B_{j+\frac{1}{2}}^{n+1}$ by

$$\begin{aligned} &M_{j+\frac{1}{2}}^{n+1} = M_{j-\frac{1}{2}}^{n+1} + \frac{\Delta r}{2}\kappa r_j^2 \mathcal{T}^{00}\left(\boldsymbol{U}_j^{n+1}\right), \quad A_{j+\frac{1}{2}}^{n+1} = 1 - 2M_{j+\frac{1}{2}}^{n+1}/r_{j+\frac{1}{2}},\\ &\ln B_{j+\frac{1}{2}}^{n+1} = \ln B_{j-\frac{1}{2}}^{n+1} + \Delta r\left(\frac{1-A_j^{n+1}}{A_j^{n+1} r_j} + \frac{\kappa r_j}{A_j^{n+1}}\mathcal{T}^{11}\left(\boldsymbol{U}_j^{n+1}\right)\right), \quad A_j^{n+1} := \frac{1}{2}\left(A_{j-\frac{1}{2}}^{n+1} + A_{j+\frac{1}{2}}^{n+1}\right). \end{aligned}$$

`Step IV`. Update the slope $\boldsymbol{\sigma}_j^{n+1}$ component-wisely in the local characteristic variables by

$$\boldsymbol{\sigma}_j^{n+1} = \boldsymbol{R}_j \text{minmod}\left(\frac{\theta}{\Delta r}\boldsymbol{R}_j^{-1}\left(\boldsymbol{U}_j^{n+1} - \boldsymbol{U}_{j-1}^{n+1}\right), \boldsymbol{R}_j^{-1}\boldsymbol{\sigma}_j^{n+1,-}, \frac{\theta}{\Delta r}\boldsymbol{R}_j^{-1}\left(\boldsymbol{U}_{j+1}^{n+1} - \boldsymbol{U}_j^{n+1}\right)\right), \tag{3.5}$$

where $\boldsymbol{R}_j := \boldsymbol{R}(\boldsymbol{U}_j^{n+1})$, the parameter $\theta \in [1, 2)$, and

$$\boldsymbol{\sigma}_j^{n+1,-} = \frac{1}{\Delta r}\left(\boldsymbol{U}_{j+\frac{1}{2}}^{n+1,-} - \boldsymbol{U}_{j-\frac{1}{2}}^{n+1,-}\right), \quad \boldsymbol{U}_{j+\frac{1}{2}}^{n+1,-} = \boldsymbol{U}_{j+\frac{1}{2}}^{\text{RP},n} + \Delta t_n\left(\frac{\partial \boldsymbol{U}}{\partial t}\right)_{j+\frac{1}{2}}^{\text{GRP},n}.$$

The paper does not pay much attention to the treatment of singularity in the source $\boldsymbol{S}$ of (2.7) and the imposition of boundary conditions at the symmetric center $r = 0$ for the GRP scheme, the readers are referred to [14] for the details.

### *3.2 Resolution of generalized Riemann problem*

This subsection resolves the GRP (3.3) in order to get $(\partial \boldsymbol{U}/\partial t)_{j+\frac{1}{2}}^{\text{GRP},n}$ in (3.2). For the sake of convenience, the subscript $j$ and the superscript $n$ will be ignored and the local GRP

(3.3) is transformed with a linear coordinate transformation to the "non-local" GRP for (2.7) with the initial data

$$\boldsymbol{U}(0,r)=\begin{cases}\boldsymbol{U}_L+(r-r_0)\boldsymbol{U}'_L, & r<r_0,\\ \boldsymbol{U}_R+(r-r_0)\boldsymbol{U}'_R, & r>r_0,\end{cases} \tag{3.6}$$

where $\boldsymbol{U}_L,\boldsymbol{U}_R,\boldsymbol{U}'_L$ and $\boldsymbol{U}'_R$ are corresponding constant vectors. The notations $\boldsymbol{U}^{\mathrm{RP},n}_{j+1/2}$ and $(\boldsymbol{U}_t)^{\mathrm{GRP},n}_{j+1/2}$ will also be simply replaced with $\boldsymbol{U}_*$ and $(\boldsymbol{U}_t)_*$, respectively, which also denote the limiting states at $r=r_0$, as $t\to 0^+$.

Since both $A$ and $B$ are locally Lipschitz continuous, the initial structure of the solution $\boldsymbol{U}^{\mathrm{GRP}}(t,r)$ to the GRP for (2.7) with (3.6) may be determined by the solution $\boldsymbol{U}^{\mathrm{RP}}(t,r)=\boldsymbol{\omega}((r-r_0)/t;\boldsymbol{U}_L,\boldsymbol{U}_R)$ of the associated (classical) Riemann problem (RP) [1,15]

$$\begin{cases}\dfrac{\partial \boldsymbol{U}}{\partial t}+\sqrt{A_*B_*}\dfrac{\partial \boldsymbol{F}(\boldsymbol{U})}{\partial r}=0, & t>0,\\ \boldsymbol{U}(0,r)=\begin{cases}\boldsymbol{U}_L, & r<r_0,\\ \boldsymbol{U}_R, & r>r_0,\end{cases}\end{cases} \tag{3.7}$$

and

$$\lim_{t\to 0^+}\boldsymbol{U}^{\mathrm{GRP}}(t,t\lambda+r_0)=\boldsymbol{\omega}(\lambda;\boldsymbol{U}_L,\boldsymbol{U}_R),\quad r-r_0=t\lambda.$$

The local wave configuration around the singularity point $(t,r)=(0,r_0)$ of the GRP for (2.7) with (3.6) depends on the values of four constant vectors and consists of two nonlinear waves, each of which may be rarefaction or shock wave. Fig. 3.1 shows the schematic description of a local wave configuration: a rarefaction wave moving to the left and a shock to the right. Fig. 3.2 displays corresponding local wave configuration of the RP (3.7). In those schematic descriptions, $\boldsymbol{U}_*$ denotes the limiting state at $r=r_0$, as $t\to 0^+$, and $\alpha$ and $\beta$ are characteristic coordinate within the rarefaction wave and will be introduced in Section 3.2.1.

Although there are other local wave configurations, we will restrict our discussion to the local wave configuration shown in Figs. 3.1 and 3.2. Other local wave configurations can be dealt with similarly and are considered in the code. The solutions to the GRP inside the left, intermediate and right subregions are denoted by $\boldsymbol{U}_L(t,r)$, $\boldsymbol{U}_*(t,r)$, and $\boldsymbol{U}_R(t,r)$, respectively. For any variable $V$, which may be $\boldsymbol{U}$ or the derivatives $\boldsymbol{U}_t$ or $\boldsymbol{U}_r$ etc., the symbols $V_L$ and $V_R$ are used to denote the limiting values of $V$ as $t\to 0^+$ in the left and right subregions adjacent to $r$-axis, respectively, and $V_*$ is used to denote the limiting values of $V$ as $t\to 0^+$ in the intermediate subregions. The main task of the direct Eulerian

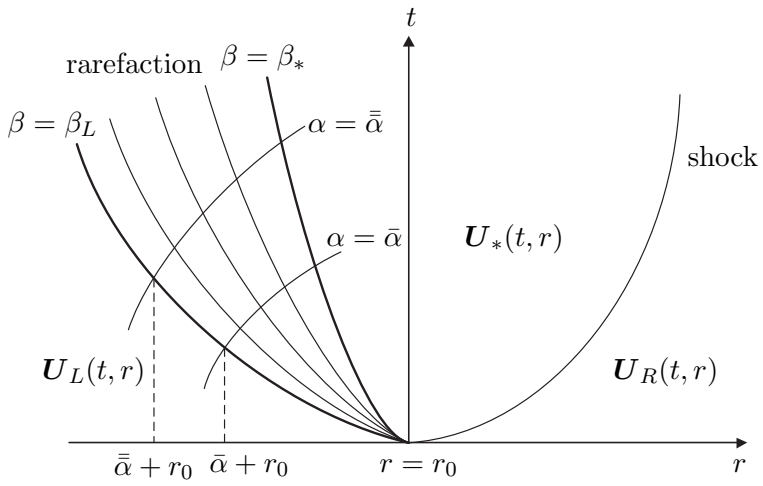


Fig. 3.1. The schematic description of a local wave configuration for the GRP for (2.7) with (3.6) with $0 \leq t \ll 1$.

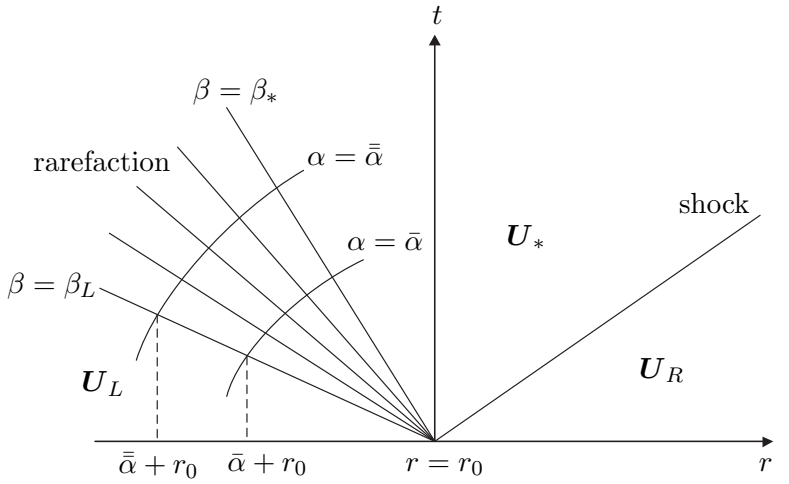


Fig. 3.2. The schematic description of a local wave configuration for the associated (classical) Riemann problem (3.7).

GRP scheme is to form a linear algebraic system

$$\begin{cases} a_L \left(\dfrac{\partial \rho}{\partial t}\right)_* + b_L \left(\dfrac{\partial v}{\partial t}\right)_* = d_L, \\ a_R \left(\dfrac{\partial \rho}{\partial t}\right)_* + b_R \left(\dfrac{\partial v}{\partial t}\right)_* = d_R, \end{cases} \tag{3.8}$$

by resolving the left wave and the right wave as shown in Figure 3.1, respectively. Solving this system gives the values of the derivatives $(\partial\rho/\partial t)_*$ and $(\partial v/\partial t)_*$, and closes the calculation in (3.2).

### 3.2.1 *Resolution of the rarefaction wave*

This section resolves the left rarefaction wave shown in Figure 3.1 for the GRP (2.7) and (3.6), and gets the first equation in (3.8).

The relation (2.15) for the Riemann invariant $\psi_-$ will be used to resolve the left rarefaction wave by tracking the directional derivatives $\frac{D_-\psi_-}{Dt}$ in the rarefaction fan. For this purpose, a local coordinate transformation is first introduced within the rarefaction wave, i.e. the characteristic coordinates, similar to those in [4,12,40]. The region of the left rarefaction wave can be described by the set $\mathcal{R} := \Big\{\big(\alpha(t,r),\beta(t,r)\big)|\beta \in [\beta_L,\beta_*], -\infty < \alpha \leq 0\Big\}$, where $\beta_L = \lambda_-(\boldsymbol{U}_L)$ and $\beta_* = \lambda_-(\boldsymbol{U}_*)$, and $\beta = \beta(t,r)$ and $\alpha = \alpha(t,r)$ are the integral curves of the following equations

$$\frac{dr}{dt} = \lambda_-, \quad \frac{dr}{dt} = \lambda_+, \tag{3.9}$$

respectively. Here $\beta$ and $\alpha$ have been denoted as follows: $\beta$ is the initial value of the slope $\lambda_-$ at the singularity point $(t,r) = (0,r_0)$, and $\alpha + r_0$ for the transversal characteristic curves is the $r$-coordinate of the intersection point with the leading $\beta$-curve, see Figure 3.1. In this case, due to the local transformation between $(t,r)$ and $(\alpha,\beta)$, all physical quantities can be considered as functions of the local coordinates $(\alpha,\beta)$ and the limiting states at $(t,r) = (0,0+)$ may be represented as $\boldsymbol{U}_* = \boldsymbol{U}(0,\beta_*)$, etc. On the other hand, the coordinates $(t,r)$ inside the left rarefaction fan shown in Figure 3.1 can be expressed in terms of $\alpha$ and $\beta$ as follows

$$t = t(\alpha,\beta), \quad r = r(\alpha,\beta).$$

Using the equations in (3.9) gives

$$\frac{\partial r}{\partial \alpha} = \lambda_- \frac{\partial t}{\partial \alpha}, \quad \frac{\partial r}{\partial \beta} = \lambda_+ \frac{\partial t}{\partial \beta}, \tag{3.10}$$

which respectively imply

$$\frac{\partial}{\partial \alpha} = \frac{\partial t}{\partial \alpha}\frac{D_-}{Dt}, \quad \frac{\partial}{\partial \beta} = \frac{\partial t}{\partial \beta}\frac{D_+}{Dt}. \tag{3.11}$$

Differentiating the first equation in (3.10) with respect to $\beta$ and the second with respect to $\alpha$ may further give

$$\frac{\partial^2 t}{\partial \alpha \partial \beta} = \frac{1}{\lambda_+ - \lambda_-}\left(\frac{\partial \lambda_-}{\partial \beta}\frac{\partial t}{\partial \alpha} - \frac{\partial \lambda_+}{\partial \alpha}\frac{\partial t}{\partial \beta}\right). \tag{3.12}$$

At $\alpha = 0$, the definition of the characteristic coordinates yields

$$\frac{\partial \lambda_-}{\partial \beta}(0,\beta) = 1, \quad \frac{\partial t}{\partial \beta}(0,\beta) = 0, \quad \forall \beta \in [\beta_L, \beta_*]. \tag{3.13}$$

With the above two relations, setting $\alpha = 0$ in (3.12) gives

$$\frac{\partial^2 t}{\partial \alpha \partial \beta}(0,\beta) = \frac{1}{\lambda_+(0,\beta) - \lambda_-(0,\beta)} \frac{\partial t}{\partial \alpha}(0,\beta). \tag{3.14}$$

Our main result is given in following theorem.

**Theorem 3.1** *The limiting values* $\left(\frac{\partial \rho}{\partial t}\right)_*$ *and* $\left(\frac{\partial v}{\partial t}\right)_*$ *satisfy*

$$a_L \left(\frac{\partial \rho}{\partial t}\right)_* + b_L \left(\frac{\partial v}{\partial t}\right)_* = d_L, \tag{3.15}$$

*where*

$$a_L = \left(\frac{c_s}{\rho + p}\right)_*, \quad b_L = \left(\frac{1}{1 - v^2}\right)_*, \tag{3.16}$$

*and*

$$\begin{aligned} d_L = &\left(\frac{\lambda_+}{\lambda_+ - \lambda_-}\right)_* \left(\frac{D_- \psi_-}{Dt}\right)_L \exp\left(-\int_{\beta_L}^{\beta_*} \frac{d\hat{\beta}}{\lambda_+(0,\hat{\beta}) - \lambda_-(0,\hat{\beta})}\right) - \left(\frac{\lambda_- s_-}{\lambda_+ - \lambda_-}\right)_* \\ &+ \left(\frac{\lambda_+}{\lambda_+ - \lambda_-}\right)_* \int_{\beta_L}^{\beta_*} \left(\frac{s_-}{\lambda_+ - \lambda_-}\right)(0,\hat{\beta}) \exp\left(-\int_{\hat{\beta}}^{\beta_*} \frac{d\omega}{\lambda_+(0,\omega) - \lambda_-(0,\omega)}\right) d\hat{\beta}, \end{aligned} \tag{3.17}$$

*is a function of the initial data* $\boldsymbol{U}_L, \boldsymbol{U}'_L$*, and the limiting values* $\boldsymbol{U}_*$ *or* $\boldsymbol{U}^{RP}$ *of the (classical) Riemann problem solution* $\boldsymbol{\omega}((r - r_0)/t, \boldsymbol{U}_L, \boldsymbol{U}_R)$*.*

**Proof** Using (2.13) and (2.15) gives

$$\begin{aligned} \frac{\lambda_+}{\lambda_+ - \lambda_-} \frac{D_- \psi_-}{Dt} &= \frac{\lambda_+}{\lambda_+ - \lambda_-} \left(\frac{\partial \psi_-}{\partial t} + \lambda_- \frac{\partial \psi_-}{\partial r}\right) \\ &= \frac{\partial \psi_-}{\partial t} + \frac{\lambda_-}{\lambda_+ - \lambda_-} \left(\frac{\partial \psi_-}{\partial t} + \lambda_+ \frac{\partial \psi_-}{\partial r}\right) \\ &= \frac{1}{1 - v^2} \frac{\partial v}{\partial t} + \frac{c_s}{\rho + p} \frac{\partial \rho}{\partial t} + \frac{\lambda_- s_-}{\lambda_+ - \lambda_-}, \end{aligned}$$

which yields (3.15) by transposition and setting $\alpha = 0,\ \beta = \beta_*$, with the coefficients $a_L, b_L$ given by (3.16) and

$$d_L = \left(\frac{\lambda_+}{\lambda_+ - \lambda_-}\right)_* \frac{D_- \psi_-}{Dt}(0,\beta_*) - \left(\frac{\lambda_- s_-}{\lambda_+ - \lambda_-}\right)_*. \tag{3.18}$$

Thus the following task is to complete the calculation of $\frac{D_-\psi_-}{Dt}(0,\beta_*)$ in (3.18). On the one hand, using the chain rule and (3.11) gives

$$\frac{\partial^2\psi_-}{\partial\alpha\partial\beta}=\frac{\partial}{\partial\beta}\left(\frac{\partial t}{\partial\alpha}\frac{D_-\psi_-}{Dt}\right)=\frac{\partial^2 t}{\partial\beta\partial\alpha}\frac{D_-\psi_-}{Dt}+\frac{\partial t}{\partial\alpha}\frac{\partial}{\partial\beta}\left(\frac{D_-\psi_-}{Dt}\right). \tag{3.19}$$

On the other hand, utilizing (3.11) and (2.15), one has

$$\frac{\partial^2\psi_-}{\partial\alpha\partial\beta}=\frac{\partial}{\partial\alpha}\left(\frac{\partial t}{\partial\beta}\frac{D_+\psi_-}{Dt}\right)=\frac{\partial}{\partial\alpha}\left(\frac{\partial t}{\partial\beta}s_-\right)=s_-\frac{\partial^2 t}{\partial\alpha\partial\beta}+\frac{\partial t}{\partial\beta}\frac{\partial s_-}{\partial\alpha}. \tag{3.20}$$

Combing (3.19) and (3.20), and then setting $\alpha=0$ by making use of (3.13) may give

$$\frac{\partial t}{\partial\alpha}(0,\beta)\frac{d}{d\beta}\left[\frac{D_-\psi_-}{Dt}(0,\beta)\right]=\left(s_-(0,\beta)-\frac{D_-\psi_-}{Dt}(0,\beta)\right)\frac{\partial^2 t}{\partial\beta\partial\alpha}(0,\beta),$$

which further gives a ordinary differential equation at $\alpha=0$ for $\frac{D_-\psi_-}{Dt}(0,\beta)$

$$\frac{d}{d\beta}\left[\frac{D_-\psi_-}{Dt}(0,\beta)\right]=-\frac{1}{\lambda_+-\lambda_-}\frac{D_-\psi_-}{Dt}(0,\beta)+\frac{s_-}{\lambda_+-\lambda_-},\quad \beta\in[\beta_L,\beta_*], \tag{3.21}$$

by noting (3.14). Hence $\frac{D_-\psi_-}{Dt}(0,\beta)$ can be formulated by integrating (3.21) as

$$\begin{aligned}\frac{D_-\psi_-}{Dt}(0,\beta)=&\left(\frac{D_-\psi_-}{Dt}\right)_L\exp\left(-\int_{\beta_L}^{\beta}\frac{d\hat\beta}{\lambda_+(0,\hat\beta)-\lambda_-(0,\hat\beta)}\right)\\&+\int_{\beta_L}^{\beta}\left(\frac{s_-}{\lambda_+-\lambda_-}\right)(0,\hat\beta)\exp\left(-\int_{\hat\beta}^{\beta}\frac{d\omega}{\lambda_+(0,\omega)-\lambda_-(0,\omega)}\right)d\hat\beta,\end{aligned} \tag{3.22}$$

for all $\beta\in[\beta_L,\beta_*]$. Setting $\beta=\beta_*$ in (3.22) and substituting it into (3.18) may give the expression of $d_L$ in (3.17) and complete the proof. ∎

**Remark 3.1** *If $p(\rho)=\sigma^2\rho$, one has $\lambda_-(0,\omega)=\sqrt{A_*B_*}\frac{v(0,\omega)-\sigma}{1-v(0,\omega)\sigma}=\omega$, and*

$$v(0,\omega)=\frac{\sigma+\varpi}{1+\sigma\varpi},\quad \varpi=\frac{\omega}{\sqrt{A_*B_*}},$$

*For this case, the integral $\int_{\hat\beta}^{\beta}\frac{d\omega}{\lambda_+(0,\omega)-\lambda_-(0,\omega)}$ in (3.22) can be expressed as*

$$\begin{aligned}\int_{\hat\beta}^{\beta}\frac{d\omega}{\lambda_+(0,\omega)-\lambda_-(0,\omega)}&=\frac{1}{2\sigma}\int_{\hat\beta/\sqrt{A_*B_*}}^{\beta/\sqrt{A_*B_*}}\frac{\sigma^2+1+2\sigma\varpi}{1-\varpi^2}d\varpi\\&=\frac{1}{4\sigma}\Big[(\sigma-1)^2\ln(1+\varpi)-(\sigma+1)^2\ln(1-\varpi)\Big]_{\varpi=\hat\beta/\sqrt{A_*B_*}}^{\varpi=\beta/\sqrt{A_*B_*}}.\end{aligned}$$

**Remark 3.2** *If the right rarefaction wave associated with the eigenvalue $\lambda_+$ appears in the GRP, then the above derivation can be used by the "reflective symmetry" transformation*

$$\rho(r,t)=\tilde{\rho}(-r,t),\quad v(r,t)=-\tilde{v}(-r,t),\quad p(r,t)=\tilde{p}(-r,t), \tag{3.23}$$

*where $(\rho,v,p)^T$ and $(\tilde{\rho},\tilde{v},\tilde{p})^T$ denote the primitive variables before and after the reflective transformation, respectively. Specially, the "reflective symmetry" transformation is first used to transfer the "real" right rarefaction wave into a "virtual" left rarefaction wave, Theorem 3.1 is then directly applied to the "virtual" left rarefaction wave, and finally using inverse transformation gives the linear equation of $\left(\frac{\partial\rho}{\partial t}\right)_*$ and $\left(\frac{\partial v}{\partial t}\right)_*$ for the right rarefaction wave.*

### *3.2.2 Resolution of the shock wave*

This section resolves the right shock wave for the GRP (2.7) and (3.6) in Figure 3.1 and gives the second equation in (3.8) through differentiating the shock relation along the shock trajectory.

Let $r=r_s(t)$ be the shock trajectory which is associated with the $\lambda_+$–characteristic field, and assume that it propagates with the speed $s:=r_s'(t)>0$ to the right, see Figure 3.1. Denote the left and right states of the shock wave by $\boldsymbol{U}(t)$ and $\overline{\boldsymbol{U}}(t)$, respectively, i.e. $\boldsymbol{U}(t)=\boldsymbol{U}\big(t,r_s(t)-0\big)$ and $\overline{\boldsymbol{U}}(t)=\boldsymbol{U}\big(t,r_s(t)+0\big)$. The Rankine-Hugoniot relation across the shock wave is

$$\left[\sqrt{AB}\boldsymbol{F}(\boldsymbol{U})\right]=s\left[\boldsymbol{U}\right], \tag{3.24}$$

or equivalently,

$$\left[\boldsymbol{F}(\boldsymbol{U})\right]=(s/\sqrt{AB})\left[\boldsymbol{U}\right], \tag{3.25}$$

where $[\cdot]$ denotes the jump across the shock wave, and the continuity of $\sqrt{AB}$ has been used. Utilizing this relation gives

$$\frac{v-\bar{v}}{1-v\bar{v}}=\Phi(\rho,\bar{\rho}), \tag{3.26}$$

where

$$\Phi(\rho,\bar{\rho}):=\sqrt{\frac{(p-\bar{p})(\rho-\bar{\rho})}{(\rho+\bar{p})(\bar{\rho}+p)}}, \tag{3.27}$$

see [11] for the detailed derivation. Thus along the shock trajectory, one always has

$$\frac{D_s}{Dt}\left(\frac{v-\bar{v}}{1-v\bar{v}}\right)=\frac{D_s}{Dt}\Phi(\rho,\bar{\rho}), \tag{3.28}$$

where $\frac{D_s}{Dt}:=\frac{\partial}{\partial t}+s\frac{\partial}{\partial x}$ denotes the directional derivative along the shock trajectory.

The main result in this subsection is given as follows.

**Theorem 3.2** *The limiting values of* $\left(\frac{\partial \rho}{\partial t}\right)_*$ *and* $\left(\frac{\partial v}{\partial t}\right)_*$ *satisfy*

$$a_R \left(\frac{\partial \rho}{\partial t}\right)_* + b_R \left(\frac{\partial v}{\partial t}\right)_* = d_R, \tag{3.29}$$

*where the expressions of the coefficients* $a_R, b_R,$ *and* $d_R$ *will be given in the proof.*

**Proof** Utilizing (2.14), one has

$$\begin{aligned}
&\begin{pmatrix} v^2 - c_s^2 - \frac{sv(1-c_s^2)}{\sqrt{AB}} & \frac{s(\rho+p)}{\sqrt{AB}} \\ \frac{s(1-v^2)^2 c_s^2}{\sqrt{AB}(\rho+p)} & v^2 - c_s^2 - \frac{sv(1-c_s^2)}{\sqrt{AB}} \end{pmatrix} \frac{\partial \boldsymbol{V}}{\partial t} \\
&= \left(v^2 - c_s^2\right) \frac{\partial \boldsymbol{V}}{\partial t} - \frac{s}{\sqrt{AB}} \begin{pmatrix} v(1-c_s^2) & -(\rho+p) \\ -\frac{(1-v^2)^2 c_s^2}{(\rho+p)} & v(1-c_s^2) \end{pmatrix} \frac{\partial \boldsymbol{V}}{\partial t} \\
&= \left(v^2 - c_s^2\right) \frac{\partial \boldsymbol{V}}{\partial t} - \frac{s}{\sqrt{AB}} \begin{pmatrix} v(1-c_s^2) & -(\rho+p) \\ -\frac{(1-v^2)^2 c_s^2}{(\rho+p)} & v(1-c_s^2) \end{pmatrix} \left(\boldsymbol{H} - \boldsymbol{J}\frac{\partial \boldsymbol{V}}{\partial r}\right) \\
&= \left(v^2 - c_s^2\right) \left(\frac{\partial \boldsymbol{V}}{\partial t} + s\frac{\partial \boldsymbol{V}}{\partial r}\right) - \frac{s}{\sqrt{AB}} \begin{pmatrix} v(1-c_s^2)H_1 - (\rho+p)H_2 \\ -\frac{(1-v^2)^2 c_s^2}{(\rho+p)} H_1 + v(1-c_s^2)H_2 \end{pmatrix} \\
&= \left(v^2 - c_s^2\right) \frac{D_s \boldsymbol{V}}{Dt} + \frac{s}{r} \begin{pmatrix} (\rho+p)\left(2v^2 - \frac{(1-A)(1-v^2)}{2A} - \frac{\kappa r^2(p+\rho v^2)}{2A}\right) \\ v(v^2-1)\left(2c_s^2 - \frac{(1-A)(1-c_s^2)}{2A} - \frac{\kappa r^2(p+\rho c_s^2)}{2A}\right) \end{pmatrix} \\
&=: \left(v^2 - c_s^2\right) \frac{D_s \boldsymbol{V}}{Dt} + (\Pi_1, \Pi_2)^{\mathrm{T}},
\end{aligned} \tag{3.30}$$

with which a relation between $\frac{\partial}{\partial t}$ and $\frac{D_s}{Dt}$ is established. The following will expand (3.28) by the chain rule and use the relation (3.30) to transfer the derivatives along the shock trajectory to the time derivatives for the left state of the shock wave. The left and right hand sides of (3.28) will be treated separately.

The left hand side of (3.28) can be rewritten as

$$\frac{D_s}{Dt}\left(\frac{v-\bar{v}}{1-v\bar{v}}\right) = \frac{1-\bar{v}^2}{(1-v\bar{v})^2}\frac{D_s v}{Dt} - \frac{1-v^2}{(1-v\bar{v})^2}\frac{D_s \bar{v}}{Dt}.$$

If considering $p$ as a function of $\rho$, i.e. $p = p(\rho)$, then the right hand side of (3.28) may

be expanded as

$$\frac{D_s}{Dt}\Phi(\rho,\bar{\rho}) = \Phi_\rho(\rho,\bar{\rho})\frac{D_s\rho}{Dt} + \Phi_{\bar{\rho}}(\rho,\bar{\rho})\frac{D_s\bar{\rho}}{Dt},$$

where

$$\Phi_\rho(\rho,\bar{\rho}) = \frac{(\bar{\rho}+\bar{p})\left(c_s^2\Delta_{\rho,\bar{\rho}}^{-1}(\rho+\bar{p}) + \Delta_{\rho,\bar{\rho}}(\bar{\rho}+p)\right)}{2\left((\rho+\bar{p})(\bar{\rho}+p)\right)^{\frac{3}{2}}},$$
$$\Phi_{\bar{\rho}}(\rho,\bar{\rho}) = -\frac{(\rho+p)\left(\bar{c}_s^2\Delta_{\rho,\bar{\rho}}^{-1}(\bar{\rho}+p) + \Delta_{\rho,\bar{\rho}}(\rho+\bar{p})\right)}{2\left((\rho+\bar{p})(\bar{\rho}+p)\right)^{\frac{3}{2}}},$$

with $\Delta_{\rho,\bar{\rho}} := \sqrt{(p-\bar{p})/(\rho-\bar{\rho})}$. Therefore, (3.28) is equivalent to

$$\Phi_\rho(\rho,\bar{\rho})\frac{D_s\rho}{Dt} + \frac{\bar{v}^2-1}{(1-v\bar{v})^2}\frac{D_sv}{Dt} = \frac{v^2-1}{(1-v\bar{v})^2}\frac{D_s\bar{v}}{Dt} - \Phi_{\bar{\rho}}(\rho,\bar{\rho})\frac{D_s\bar{\rho}}{Dt}. \tag{3.31}$$

Multiplying both sides of (3.30) with the row vector $\left(\Phi_\rho(\rho,\bar{\rho}), \frac{\bar{v}^2-1}{(1-v\bar{v})^2}\right)$, and then substituting (3.31) into it, we have

$$\begin{aligned}
&\left(\Phi_\rho(\rho,\bar{\rho}), \frac{\bar{v}^2-1}{(1-v\bar{v})^2}\right)\begin{pmatrix} v^2-c_s^2-\frac{sv(1-c_s^2)}{\sqrt{AB}} & \frac{s(\rho+p)}{\sqrt{AB}} \\ \frac{s(1-v^2)^2c_s^2}{\sqrt{AB}(\rho+p)} & v^2-c_s^2-\frac{sv(1-c_s^2)}{\sqrt{AB}}\end{pmatrix}\frac{\partial \boldsymbol{V}}{\partial t} \\
&= (v^2-c_s^2)\left(\Phi_\rho(\rho,\bar{\rho})\frac{D_s\rho}{Dt} + \frac{\bar{v}^2-1}{(1-v\bar{v})^2}\frac{D_sv}{Dt}\right) + \Phi_\rho(\rho,\bar{\rho})\Pi_1 + \frac{\bar{v}^2-1}{(1-v\bar{v})^2}\Pi_2 \\
&= (v^2-c_s^2)\left(\frac{v^2-1}{(1-v\bar{v})^2}\frac{D_s\bar{v}}{Dt} - \Phi_{\bar{\rho}}(\rho,\bar{\rho})\frac{D_s\bar{\rho}}{Dt}\right) + \Phi_\rho(\rho,\bar{\rho})\Pi_1 + \frac{\bar{v}^2-1}{(1-v\bar{v})^2}\Pi_2.
\end{aligned} \tag{3.32}$$

Setting $t \to 0^+$ in (3.32) gives (3.29) with

$$a_R = \Phi_\rho(\rho_*,\rho_R)\left(v^2-c_s^2-\frac{sv(1-c_s^2)}{\sqrt{AB}}\right)_* + \frac{v_R^2-1}{(1-v_*v_R)^2}\left(\frac{s(1-v^2)^2c_s^2}{\sqrt{AB}(\rho+p)}\right)_*, \tag{3.33}$$

$$b_R = \Phi_\rho(\rho_*,\rho_R)\frac{s_*(\rho_*+p_*)}{\sqrt{A_*B_*}} + \frac{v_R^2-1}{(1-v_*v_R)^2}\left(v^2-c_s^2-\frac{sv(1-c_s^2)}{\sqrt{AB}}\right)_*, \tag{3.34}$$

and

$$\begin{aligned}
d_R =& \Phi_\rho(\rho_*,\rho_R)(\Pi_1)_* + \frac{v_R^2-1}{(1-v_*v_R)^2}(\Pi_2)_* \\
&+ (v^2-c_s^2)_*\left[\frac{v_*^2-1}{(1-v_*v_R)^2}\left(\frac{D_sv}{Dt}\right)_R - \Phi_{\bar{\rho}}(\rho_*,\rho_R)\left(\frac{D_s\rho}{Dt}\right)_R\right],
\end{aligned}$$

where $s_*$ denotes the initial value of the slope of the shock trajectory. The proof is completed. ∎

**Remark 3.3** *Similarly, if the left shock wave associated with the eigenvalue $\lambda_-$ appears in the GRP, then Theorem 3.2 may be applied to the "virtual" right shock wave obtained by using the "reflective symmetry" transformation (3.23), and corresponding inverse transformation is finally used to give the linear equation of the limiting values $\left(\frac{\partial \rho}{\partial t}\right)_*$ and $\left(\frac{\partial v}{\partial t}\right)_*$.*

### *3.2.3 Time derivatives of solutions at singularity point*

This subsection is devoted to derive the time derivatives $(\partial \boldsymbol{U}/\partial t)_*$ and complete the calculation in (3.2).

*I. Nonsonic case*

The discussion in this part is only restricted to the case of the local wave configuration in Fig. 3.1, in which $\lambda_-(\boldsymbol{U}_*) < 0$, that is to say, the $t$-axis locates at the right hand side of the rarefaction wave. Other (possible) nonsonic local wave configurations can be similarly discussed and should be implemented in the code, while the case of the transonic rarefaction wave will be discussed later.

**Theorem 3.3** *Under the assumption that $\lambda_-(\boldsymbol{U}_*) < 0$ and $s_* > 0$, the $2\times 2$ linear system formed by (3.15) in Theorem 3.1 and (3.29) in Theorem 3.2 has unique solution.*

**Proof** It only needs to check

$$\det\begin{pmatrix} a_L & b_L \\ a_R & b_R \end{pmatrix} = a_L b_R - a_R b_L \neq 0,$$

which is sufficiently ensured if $a_L b_L a_R b_R < 0$. It is obvious that $a_L b_L > 0$ due to (3.16). Thus if $a_R b_R < 0$, then the proof may be completed. Before that, we first prove the following inequality

$$\left(v^2 - c_s^2 - \frac{sv(1-c_s^2)}{\sqrt{AB}}\right)_* < 0. \tag{3.35}$$

The Lax entropy inequality for the right shock wave

$$\left(\sqrt{AB}\frac{v+c_s}{1+vc_s}\right)_* > s_* > \left(\sqrt{AB}\frac{v+c_s}{1+vc_s}\right)_R, \tag{3.36}$$

implies $(v+c_s)_* > 0$ due to $s_* > 0$. If $v_* \leq 0$, with the left inequality in (3.36), one has

$$\left(\frac{sv(1-c_s^2)}{\sqrt{AB}}\right)_* \geq \left(\frac{(v+c_s)v(1-c_s^2)}{1+vc_s}\right)_* = \left(v^2 - c_s^2 + \frac{c_s(v+c_s)(1-v^2)}{1+vc_s}\right)_* > (v^2-c_s^2)_*,$$

where $(v+c_s)_*>0$ has been used in the last inequality. If $v_*>0$, then one has

$$\left(v^2-c_s^2-\frac{sv(1-c_s^2)}{\sqrt{AB}}\right)_*<(v^2-c_s^2)_*=\lambda_-(\boldsymbol{U}_*)\,(v+c_s)_*\left(\frac{1-vc_s}{\sqrt{AB}}\right)_*<0,$$

where $\lambda_-(\boldsymbol{U}_*)<0$ and $(v+c_s)_*>0$ have been used in the last inequality. Hence the inequality (3.35) holds for any $v_*$. The expressions of $a_R$ in (3.33) and $b_R$ in (3.34), and $v_R<1$ and $\Phi_\rho(\rho_*,\rho_R)>0$ imply that $a_R<0$ and $b_R>0$. Therefore $a_Lb_La_Rb_R<0$ and the proof is completed. ∎

*II. Sonic case*

Next, discuss the sonic case of that the $t$-axis is within the left rarefaction region in Fig. 3.1. In this case, the $t$-axis is actually tangential to the $\lambda_-$-characteristic curve with zero initial slope, i.e. $\lambda_-(0,\beta_*)=0$ or $\beta_*=0$. Then one has

$$\left(\frac{\partial\boldsymbol{U}}{\partial t}\right)_*=\frac{D_-\boldsymbol{U}}{Dt}(0,\beta_*),$$

for $\beta_*=0$.

**Theorem 3.4** *If the $t$-axis is (locally) located inside the left rarefaction wave, then one has*

$$\left(\frac{\partial\rho}{\partial t}\right)_*=\left(\frac{\rho+p}{2c_s}\right)_*\left(\frac{D_-\psi_-}{Dt}(0,\beta_*)-(s_+)_*\right),\tag{3.37}$$

$$\left(\frac{\partial v}{\partial t}\right)_*=\frac{1-v_*^2}{2}\left(\frac{D_-\psi_-}{Dt}(0,\beta_*)+(s_+)_*\right),\tag{3.38}$$

*with $\beta_*=0$, where $\frac{D_-\psi_-}{Dt}(0,\beta_*)$ can be calculated by setting $\beta=\beta_*$ in (3.22).*

**Proof** From (2.15), for $\alpha=0,\beta_*=0$, one has

$$\left(\frac{1}{1-v^2}\frac{\partial v}{\partial t}-\frac{c_s}{\rho+p}\frac{\partial\rho}{\partial t}\right)_*=\left(\frac{1}{1-v^2}\frac{D_-v}{Dt}-\frac{c_s}{\rho+p}\frac{D_-\rho}{Dt}\right)_*=(s_+)_*.\tag{3.39}$$

On the other hand, the expression of $\psi_-$ in (2.13) yields

$$\left(\frac{1}{1-v^2}\frac{\partial v}{\partial t}+\frac{c_s}{\rho+p}\frac{\partial\rho}{\partial t}\right)_*=\frac{\partial\psi_-}{\partial t}(0,\beta_*)=\frac{D_-\psi_-}{Dt}(0,\beta_*).\tag{3.40}$$

Combining (3.39) and (3.40) may give (3.37) and (3.38), and complete the proof. ∎

As soon as the limiting values of the time derivatives $(\partial\rho/\partial t)_*$ and $(\partial v/\partial t)_*$ are obtained, the limiting values of the time derivatives for conservative variable vector $\boldsymbol{U}$ can be calculated by the chain rule as follows

$$\left(\frac{\partial \boldsymbol{U}}{\partial t}\right)_* = \begin{pmatrix} ((1+c_s^2)W^2 - c_s^2)\,\frac{\partial \rho}{\partial t} + 2vW^4(\rho+p)\frac{\partial v}{\partial t} \\ (1+c_s^2)W^2 v\frac{\partial \rho}{\partial t} + W^4(1+v^2)(\rho+p)\frac{\partial v}{\partial t} \end{pmatrix}_*.$$

### *3.2.4 Acoustic case*

This section discusses the acoustic case of the GRP (2.7) and (3.6), i.e. $\boldsymbol{U}_L = \boldsymbol{U}_R$ and $\boldsymbol{U}'_L \neq \boldsymbol{U}'_R$. In this case, $\boldsymbol{U}_L = \boldsymbol{U}_* = \boldsymbol{U}_R$ and only linear waves emanate from the origin (0,0) so that the resolution of the GRP becomes simpler than the general case discussed before, see Theorem 3.5. For the sake of simplicity, the subscripts $L$, $R$, and $*$ of the variables $\boldsymbol{U}$ or $\boldsymbol{V}$ etc. will be omitted because $\boldsymbol{U}_L = \boldsymbol{U}_* = \boldsymbol{U}_R$.

**Theorem 3.5** *If $\lambda_- < 0$ and $\lambda_+ > 0$, then $(\partial\rho/\partial t)_*$ and $(\partial v/\partial t)_*$ can be obtained by*

$$\left(\frac{\partial \rho}{\partial t}\right)_* = -\frac{1}{2}\left[\lambda_+\rho'_L + \lambda_-\rho'_R + \frac{\rho+p}{c_s(1-v^2)}\left(\lambda_+ v'_L - \lambda_- v'_R\right)\right] + H_1, \tag{3.41}$$

$$\left(\frac{\partial v}{\partial t}\right)_* = -\frac{1}{2}\left[\lambda_+ v'_L + \lambda_- v'_R + \frac{c_s(1-v^2)}{\rho+p}\left(\lambda_+\rho'_L - \lambda_-\rho'_R\right)\right] + H_2. \tag{3.42}$$

**Proof** Since the solution $\rho(t,r)$ is continuous across the $\lambda_-$ characteristic curves, the directional derivative along the trajectory $r'(t) = \lambda_-$ of the variable $\rho$ satisfies

$$\begin{aligned}\left(\frac{D_-\rho}{Dt}\right)_* &= \left(\frac{\partial \rho}{\partial t}\right)_L + \lambda_-\left(\frac{\partial \rho}{\partial x}\right)_L \\ &= -\frac{\sqrt{AB}}{1-v^2c_s^2}\left[v(1-c_s^2)\left(\frac{\partial \rho}{\partial x}\right)_L + (\rho+p)\left(\frac{\partial v}{\partial x}\right)_L\right] + H_1 + \lambda_-\left(\frac{\partial \rho}{\partial x}\right)_L \\ &= -\frac{\sqrt{AB}}{1-v^2c_s^2}\left[c_s(1-v^2)\left(\frac{\partial \rho}{\partial x}\right)_L + (\rho+p)\left(\frac{\partial v}{\partial x}\right)_L\right] + H_1,\end{aligned} \tag{3.43}$$

here the first equation in (2.14) has been used. Similarly, the directional derivative along the trajectory $r'(t) = \lambda_+$ of the variable $\rho$ may be calculated by

$$\begin{aligned}\left(\frac{D_+\rho}{Dt}\right)_* &= \left(\frac{\partial \rho}{\partial t}\right)_R + \lambda_+\left(\frac{\partial \rho}{\partial x}\right)_R \\ &= -\frac{\sqrt{AB}}{1-v^2c_s^2}\left[v(1-c_s^2)\left(\frac{\partial \rho}{\partial x}\right)_R + (\rho+p)\left(\frac{\partial v}{\partial x}\right)_R\right] + H_1 + \lambda_+\left(\frac{\partial \rho}{\partial x}\right)_R\end{aligned}$$

$$= -\frac{\sqrt{AB}}{1-v^2c_s^2}\left[c_s(v^2-1)\left(\frac{\partial \rho}{\partial x}\right)_R + (\rho+p)\left(\frac{\partial v}{\partial x}\right)_R\right] + H_1. \tag{3.44}$$

Substituting (3.43) and (3.44) into

$$\left(\frac{\partial \rho}{\partial t}\right)_* = \frac{1}{\lambda_+ - \lambda_-}\left(\lambda_+ \frac{D_-\rho}{Dt} - \lambda_- \frac{D_+\rho}{Dt}\right)_*$$

may yield (3.41). Since the solution $v(t,r)$ is continuous across the $\lambda_-$ characteristic curves, it holds by the second equation in (2.14) that

$$\begin{aligned}\left(\frac{D_- v}{Dt}\right)_* &= \left(\frac{\partial v}{\partial t}\right)_L + \lambda_- \left(\frac{\partial v}{\partial x}\right)_L \\ &= -\frac{\sqrt{AB}}{1-v^2c_s^2}\left[\frac{(1-v^2)^2c_s^2}{\rho+p}\left(\frac{\partial \rho}{\partial x}\right)_L + v(1-c_s^2)\left(\frac{\partial v}{\partial x}\right)_L\right] + H_2 + \lambda_-\left(\frac{\partial v}{\partial x}\right)_L \\ &= -\frac{\sqrt{AB}}{1-v^2c_s^2}\left[\frac{(1-v^2)^2c_s^2}{\rho+p}\left(\frac{\partial \rho}{\partial x}\right)_L + c_s(1-v^2)\left(\frac{\partial v}{\partial x}\right)_L\right] + H_2, \end{aligned} \tag{3.45}$$

Similarly, the directional derivative along the trajectory $r'(t) = \lambda_+$ of the variable $v$ is given by

$$\begin{aligned}\left(\frac{D_+ v}{Dt}\right)_* &= \left(\frac{\partial v}{\partial t}\right)_R + \lambda_+ \left(\frac{\partial v}{\partial x}\right)_R \\ &= -\frac{\sqrt{AB}}{1-v^2c_s^2}\left[\frac{(1-v^2)^2c_s^2}{\rho+p}\left(\frac{\partial \rho}{\partial x}\right)_R + v(1-c_s^2)\left(\frac{\partial v}{\partial x}\right)_R\right] + H_2 + \lambda_-\left(\frac{\partial v}{\partial x}\right)_R \\ &= -\frac{\sqrt{AB}}{1-v^2c_s^2}\left[\frac{(1-v^2)^2c_s^2}{\rho+p}\left(\frac{\partial \rho}{\partial x}\right)_R + c_s(v^2-1)\left(\frac{\partial v}{\partial x}\right)_R\right] + H_2, \end{aligned} \tag{3.46}$$

Substituting (3.45) and (3.46) into

$$\left(\frac{\partial v}{\partial t}\right)_* = \frac{1}{\lambda_+ - \lambda_-}\left(\lambda_+ \frac{D_- v}{Dt} - \lambda_- \frac{D_+ v}{Dt}\right)_*$$

can give (3.42). The proof is completed. ∎

## 4 Numerical experiments

This section will solve several initial-boundary-value problems of the spherically symmetric general RHD equations (2.7)–(2.9) to verify the accuracy and the capability in resolving discontinuity of the GRP scheme presented in the last section, in comparison with the Godunov scheme, given in Appendix A, which is little different from but simpler than the one presented in [32]. Unless specifically stated, all computations will be

restricted to the equation of state (2.12) and the CFL number $C_{cfl} = 0.45$ (resp. 0.9) for the GRP (resp. Godunov) scheme, where $\sigma$ is a positive constant less than 1. Moreover, the parameter $\theta$ in (3.5) is taken as 1.9.

**Example 4.1 (Accretion onto a Schwarzschild black hole)** This test simulates the stationary solution of the spherical accretion onto a Schwarzschild black hole of unit mass (i.e. $M = 1$), where the Schwarzschild spacetime is considered with the line element (2.6) and

$$A(t, r) = B(t, r) = 1 - \frac{2}{r}.$$

The Einstein coupling constant $\kappa$ is taken as 0 in the spherically symmetric general RHD equations (2.7)–(2.9) and the derivation of the GRP scheme, and the parameter $\sigma$ in (2.12) is taken as 0.1. Thus the analytic steady state solution is given by

$$\rho(r) = \frac{D_0(1 - v^2)}{-vr^2 A(t, r)}, \quad v(r) = -\sqrt{\varpi(r)}, \tag{4.1}$$

where $\varpi(r)$ solves the nonlinear equation

$$(1 - \varpi)\varpi^{\frac{\sigma^2}{1-\sigma^2}} = A(t, r)\left(\frac{2}{r}\right)^{\frac{4\sigma^2}{1-\sigma^2}}.$$

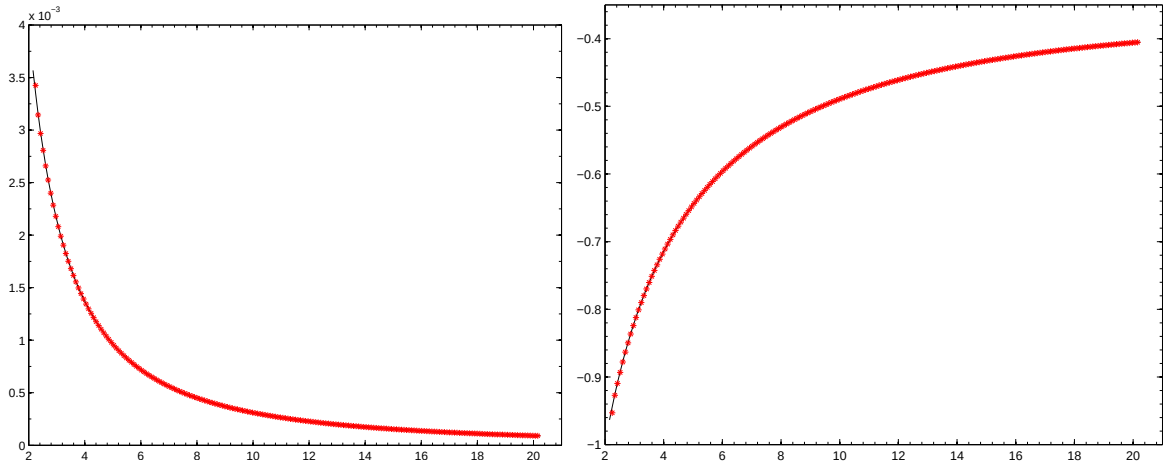


Fig. 4.1. Example 4.1: The rest energy density $\rho$ (left) and velocity $v$ (right) at $t = 160$. The numerical solutions obtained by the GRP scheme are drawn in the symbol "$*$", while the solid lines stand for the exact steady solutions.

In the computations, the parameter $D_0$ in (4.1) is taken as $1.6 \times 10^{-2}$, the initial density $\rho$ is zero everywhere and taken as a small number e.g. $10^{-8}$, and the velocity $v = 0$, except on the outer boundary where a gas is injected continuously with the exact flow variables in (4.1). Fig. 4.1 shows the numerical results at $t = 160$ given by the GRP scheme with 200 uniform cells in the computational domain $[2.2, 20.2]$. Outflow boundary conditions have

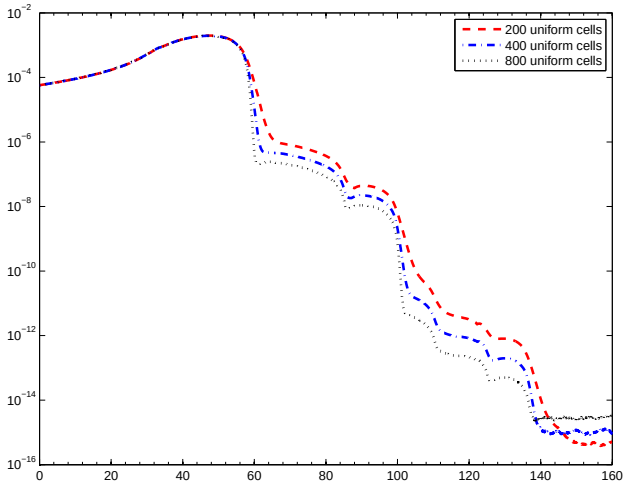


Fig. 4.2. Example 4.1: Convergence history in the residuals with respect to the time $t$ on three uniform meshes.

been specified at the inner boundary $r = 2.2$. It can be seen that the velocity approaches the speed of light when the gas approaches to the black hole, while the proposed GRP scheme exhibits good robustness. Fig. 4.2 displays the convergence history in the residuals with respect to the time $t$ on three meshes of 200, 400 and 800 uniform cells respectively. It can be seen that the correct steady solutions are obtained by the GRP scheme with the residuals less than $10^{-14}$.

Before simulating the shock wave models, we first consider several continuous models in fullly general relativistic case, which are two transformations of the Friedmann-Robertson-Walker (FRW) metrics (denoted by FRW-1 and FRW-2 respectively) and the Tolmann-Oppengeimer-Volkoff (TOV) metric presented in [31]. The exact solutions to those continuous models are smooth and may be used to test the accuracy of the proposed GRP scheme.

**Example 4.2 (FRW-1 model)** Consider the conformally flat FRW metric, where the distance measure by the line element

$$ds^2 = -d\tilde{t}^2 + R^2(\tilde{t})\left[d\tilde{r}^2 + \tilde{r}^2\left(d\theta^2 + \sin^2\theta d\phi^2\right)\right], \tag{4.2}$$

where $\tilde{t}$ is the time since the big bang, and the cosmological scale function is defined by $R(\tilde{t}) = \sqrt{\tilde{t}}$. Under the coordinate transformation [30]

$$t = \tilde{t} + \frac{\tilde{r}^2}{4}, \quad r = \tilde{r}\sqrt{\tilde{t}},$$

Eq. (4.2) goes over to (2.6) with the metric components

$$A(t,r) = 1 - v^2, \quad B(t,r) = \frac{1}{1-v^2}.$$

The exact fluid variables at $(t, r)$ are

$$\rho(t,r) = \frac{16v^2}{3(1+\sigma^2)^2\kappa r^2}, \quad v(t,r) = \frac{1-\sqrt{1-\xi^2}}{\xi}, \tag{4.3}$$

where $\kappa$ is Einstein's coupling constant, $\xi := r/t$, and $\sigma$ denotes the parameter in (2.12). This model is solved by using the proposed GRP scheme from $t = 15$ to 16 on several different uniform meshes for the spatial domain $[3, 7]$. The boundary conditions are specified at both ends by using the exact solutions (4.3) and $\sigma$ is taken as $1/\sqrt{3}$. Table 4.1 gives the numerical relative errors of $\rho, v, A$, and $B$ in $l^1$-norm and corresponding convergence rates. The results show that the numerical convergence rates in $l^1$-norm are almost $(\Delta r)^2$, in agreement with the theoretical.

Table 4.1

Example 4.2: Numerical errors in $l^1$-norm and corresponding convergence rates at $t = 16$ for the GRP scheme.

| $N$ | $\rho$ | | $v$ | | $A$ | | $B$ | |
|---|---|---|---|---|---|---|---|---|
| | error | order | error | order | error | order | error | order |
| 25 | 4.8775e-9 | – | 1.0383e-5 | – | 1.2692e-5 | – | 9.2447e-6 | – |
| 50 | 1.2695e-9 | 1.94 | 2.7667e-6 | 1.91 | 3.1843e-6 | 1.99 | 2.3011e-6 | 2.01 |
| 100 | 3.2486e-10 | 1.97 | 7.1233e-7 | 1.96 | 7.9744e-7 | 2.00 | 5.7398e-7 | 2.00 |
| 200 | 8.2267e-11 | 1.98 | 1.8094e-7 | 1.98 | 1.9952e-7 | 2.00 | 1.4334e-7 | 2.00 |
| 400 | 2.0723e-11 | 1.99 | 4.5522e-8 | 1.99 | 4.9895e-8 | 2.00 | 3.5820e-8 | 2.00 |
| 800 | 5.2016e-12 | 1.99 | 1.1409e-8 | 2.00 | 1.2476e-8 | 2.00 | 8.9526e-9 | 2.00 |
| 1600 | 1.3035e-12 | 2.00 | 2.8557e-9 | 2.00 | 3.1193e-9 | 2.00 | 2.2379e-9 | 2.00 |

**Example 4.3 (FRW-2 model)** The FRW metric can also be transformed to the standard Schwarzschild coordinates under the coordinate transformation [31]

$$t = \tilde{r}\sqrt{\tilde{t}}, \quad r = \frac{\Psi_0}{2}\sqrt{\frac{4\tilde{t}^2 + \tilde{t}\tilde{r}^2}{\tilde{t}}},$$

that is to say, the line element (4.2) is transformed to (2.6) with the metric components

$$A(t,r) = 1 - v^2, \quad B(t,r) = \frac{1}{\Psi(1-v^2)}, \tag{4.4}$$

where $\Psi(t,r) = \Psi_0\sqrt{\frac{\tilde{t}}{4\tilde{t}^2+r^2}}$, and $\Psi_0$ is a positive constant and taken as 1 in the simulation.

The exact solutions in the fluid variables corresponding to the above metric are

$$\rho(t,r) = \frac{4}{3(1+\sigma^2)^2\kappa\tilde{t}^2}, \quad v(t,r) = \frac{r}{2\tilde{t}},$$

where

$$\tilde{t} = \frac{t^2 + \sqrt{t^4 - r^2\Psi_0^4}}{2\Psi_0^2}.$$

The spherically symmetric general RHD equations (2.7)–(2.9) are solved by using the proposed GRP scheme from $t = 15$ to 16 on several different uniform meshes in the spatial interval $[3, 7]$ with the boundary conditions specified by the exact solutions. Table 4.2 lists the numerical relative errors of $\rho, v, A$, and $B$ in $l^1$-norm and corresponding convergence rates. The results show that the numerical convergence rates of the GRP scheme are almost $(\Delta r)^2$, which is the same as the theoretical, thus the numerical method is of order 2.

Table 4.2
Example 4.3: Numerical errors in $l^1$-norm and corresponding convergence rates at $t = 16$ for the GRP scheme.

| $N$ | $\rho$ | | $v$ | | $A$ | | $B$ | |
|---|---|---|---|---|---|---|---|---|
| | error | order | error | order | error | order | error | order |
| 25 | 4.9541e-7 | – | 2.7875e-4 | – | 1.0705e-4 | – | 4.9777e-5 | – |
| 50 | 1.2027e-7 | 2.04 | 6.7309e-5 | 2.05 | 2.6922e-5 | 1.99 | 1.2251e-5 | 2.02 |
| 100 | 2.9824e-8 | 2.01 | 1.6539e-5 | 2.02 | 6.7379e-6 | 2.00 | 3.0235e-6 | 2.02 |
| 200 | 7.4306e-9 | 2.00 | 4.1037e-6 | 2.01 | 1.6857e-6 | 2.00 | 7.5182e-7 | 2.01 |
| 400 | 1.8551e-9 | 2.00 | 1.0223e-6 | 2.01 | 4.2159e-7 | 2.00 | 1.8747e-7 | 2.00 |
| 800 | 4.6353e-10 | 2.00 | 2.5514e-7 | 2.00 | 1.0541e-7 | 2.00 | 4.6800e-8 | 2.00 |
| 1600 | 1.1584e-10 | 2.00 | 6.3738e-8 | 2.00 | 2.6357e-8 | 2.00 | 1.1694e-8 | 2.00 |

**Example 4.4 (TOV model)** The general relativistic version of TOV model describes the static singular isothermal spheres [28]. Two components of the TOV metrics are

$$A(t,r) = 1 - 8\pi\mathcal{G}\gamma, \quad B(t,r) = B_0 r^{\frac{4\sigma}{1+\sigma}}, \tag{4.5}$$

where the parameter $\gamma$ is related to $\sigma$ in (2.12) by

$$\gamma = \frac{1}{2\pi\mathcal{G}}\left(\frac{\sigma^2}{1+6\sigma^2+\sigma^4}\right). \tag{4.6}$$

The exact solutions in the fluid variables are given by

$$\rho(t,r) = \frac{\gamma}{r^2}, \quad v(t,r) = 0. \tag{4.7}$$

In our computations, $B_0$ and $\sigma$ are taken as 1 and $1/\sqrt{3}$, respectively.

Table 4.3
Example 4.4: Numerical errors in $l^1$-norm and corresponding convergence rates at $t = 16$ for the GRP scheme.

| $N$ | $\rho$ | | $v$ | | $A$ | | $B$ | |
|---|---|---|---|---|---|---|---|---|
| | error | order | error | order | error | order | error | order |
| 25 | 4.4342e-7 | – | 6.5575e-4 | – | 2.5962e-5 | – | 1.1524e-3 | – |
| 50 | 1.1136e-7 | 1.99 | 1.6311e-4 | 2.01 | 6.2838e-6 | 2.05 | 2.6952e-4 | 2.10 |
| 100 | 2.7877e-8 | 2.00 | 4.0716e-5 | 2.00 | 1.5688e-6 | 2.00 | 6.5011e-5 | 2.05 |
| 200 | 6.9757e-9 | 2.00 | 1.0174e-5 | 2.00 | 3.9366e-7 | 2.00 | 1.5952e-5 | 2.03 |
| 400 | 1.7449e-9 | 2.00 | 2.5427e-6 | 2.00 | 9.8718e-8 | 2.00 | 3.9504e-6 | 2.01 |
| 800 | 4.3635e-10 | 2.00 | 6.3548e-7 | 2.00 | 2.4722e-8 | 2.00 | 9.8298e-7 | 2.01 |
| 1600 | 1.0911e-10 | 2.00 | 1.5886e-7 | 2.00 | 6.1869e-9 | 2.00 | 2.4515e-7 | 2.00 |

Numerical experiments are conducted by the proposed GRP scheme from the time $t = 15$ to 16 on the different uniform meshes in the interval $[3, 7]$, where the boundary conditions are specified by using the exact solutions (4.7). Table 4.3 shows the numerical relative errors of $\rho, v, A$, and $B$ in $l^1$-norm and corresponding convergence rates. We see that the numerical convergence rates of the proposed GRP scheme are almost $(\Delta r)^2$.

**Example 4.5 (Shock wave model)** This test will simulate the general relativistic shock waves. The setup of the problem is the same as that in [32]. The initial conditions at $t = t_0$ are as follows

$$\Big(\rho(t_0,r), v(t_0,r)\Big) = \begin{cases} \Big(\frac{3v^2}{\kappa r^2}, \frac{1-\sqrt{1-\xi^2}}{\xi}\Big), & r < r_0, \\ \Big(\frac{\gamma}{r^2}, 0\Big), & r > r_0, \end{cases} \tag{4.8}$$

and

$$A(t_0,r)=\begin{cases}1-v^2, & r<r_0,\\ 1-8\pi\mathcal{G}\gamma, & r>r_0,\end{cases}$$
$$B(t_0,r)=\begin{cases}\frac{1}{1-v^2}, & r<r_0,\\ B_0 r^{\frac{4\sigma^2}{1+\sigma^2}}, & r>r_0,\end{cases} \tag{4.9}$$

which match the FRW-1 and TOV metrics if the left limiting value of the initial fluid velocity at the discontinuity $r=r_0$ from the FRW-1 side is given by

$$v_0 := v(t_0, r_0-0) = \sqrt{8\pi\mathcal{G}\gamma},$$

with the parameter $\gamma$ defined in (4.6), and the starting time $t_0$ and the parameter $B_0$ are taken as

$$t_0=\frac{r_0(1+v_0^2)}{2v_0}, \quad B_0 = r_0^{-4\sigma^2/1+\sigma^2}/(1-v_0^2),$$

respectively. In numerical computations, the computational domain is chosen as $[3,7]$, the boundary conditions are specified at $r=3$ and 7 by using the exact FRW-1 and TOV solutions (4.3) and (4.7), respectively, and the initial discontinuity is located at $r_0=5$.

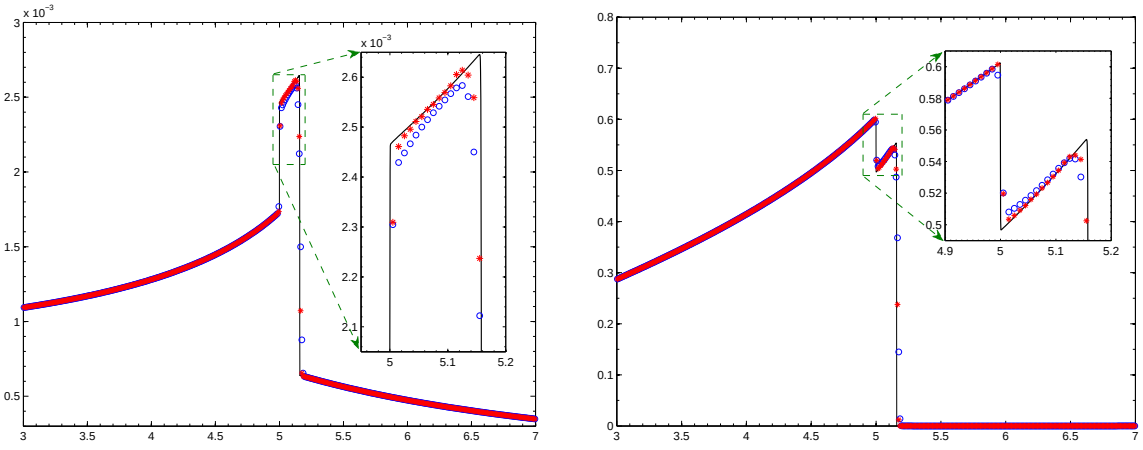

Fig. 4.3. Example 4.5: The rest energy density $\rho$ (left) and velocity $v$ (right) at $t=t_0+0.2$. The numerical solutions obtained by the Godunov and GRP schemes are drawn in the symbols "$\circ$" and "$*$", respectively, while the solid lines stand for the reference solutions given by the Godunov scheme with a fine mesh of 10000 uniform cells.

Figs. 4.3–4.5 show the numerical solutions at $t=t_0+0.2$, $t_0+0.6$, and $t_0+1$, obtained by using the first-order accurate Godunov scheme and the second-order accurate GRP scheme with 400 uniform cells, respectively. It can be seen that the results agree well with the reference solutions and the GRP scheme resolves the relativistic shock waves better than the Godunov scheme.

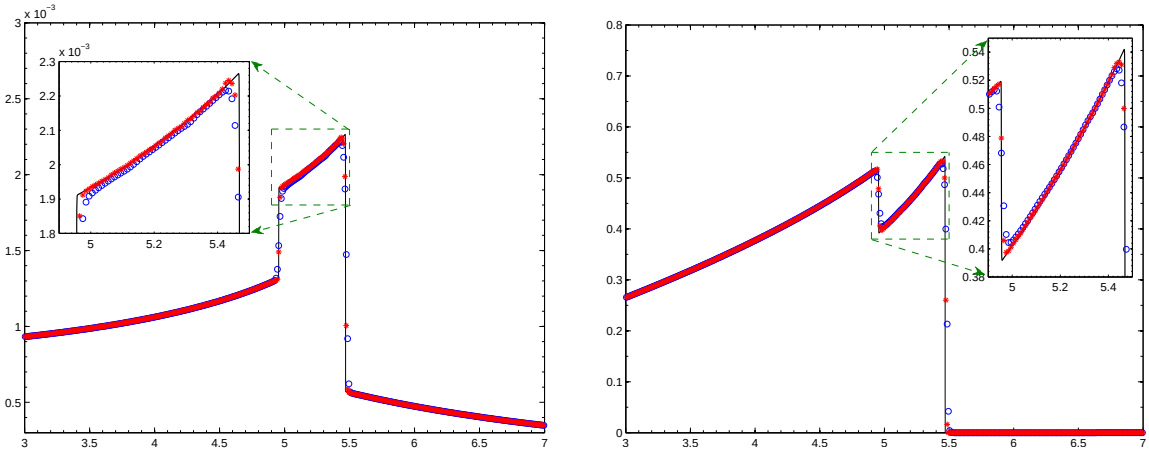

Fig. 4.4. Same as Fig. 4.3, except for the output time $t = t_0 + 0.6$.

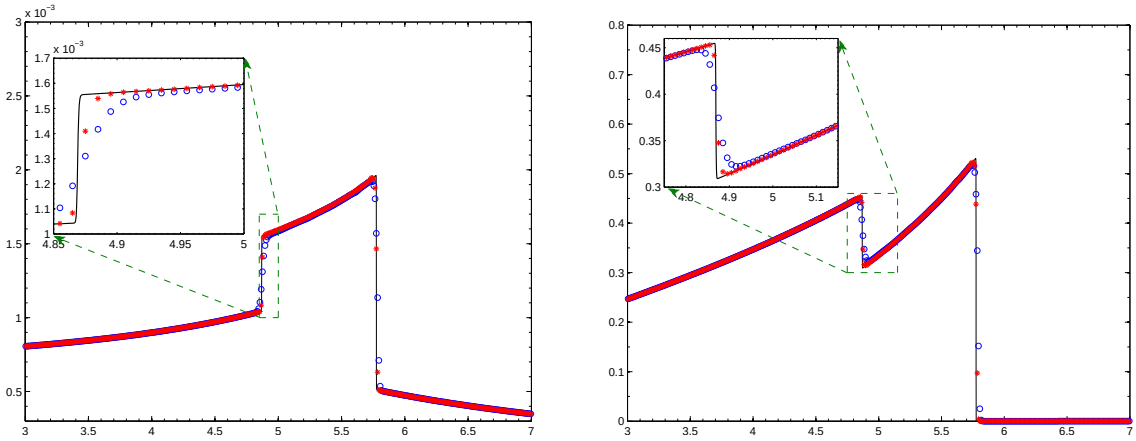

Fig. 4.5. Same as Fig. 4.3, except for $t = t_0 + 1$.

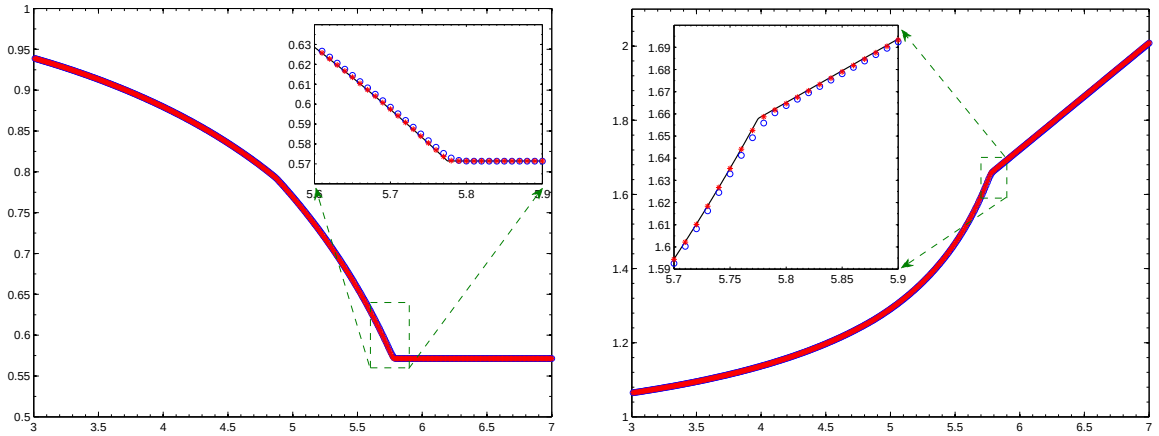

Fig. 4.6. Same as Fig. 4.3, except for the metric functions $A$ (left) and $B$ (right) at $t = t_0 + 1$.

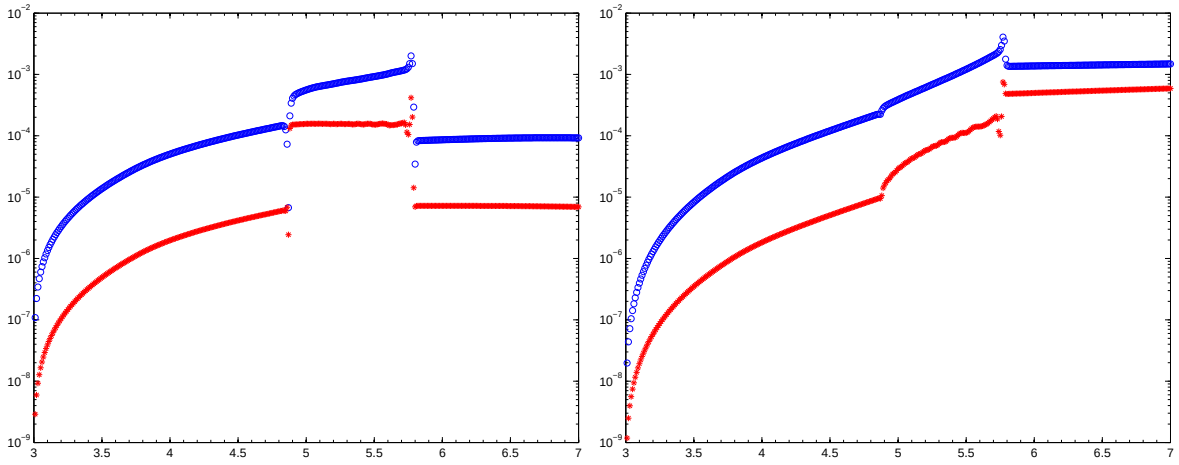

Fig. 4.7. Example 4.5: The numerical errors in the metric functions $A$ (left) and $B$ (right) at $t = t_0 + 1$. Those of the Godunov and GRP schemes are drawn in the symbols "$\circ$" and "$*$", respectively.

Figs. 4.6 and 4.7 display the numerical solutions and corresponding errors between the numerical and reference solutions in the metric functions $A$ and $B$ at $t = t_0 + 1$ by using the Godunov scheme and the GRP scheme with 400 uniform cells, respectively. These results show that the GRP scheme is much more accurate than the Godunov scheme, and the errors given by the GRP scheme is about ten percent of those computed by the Godunov scheme.

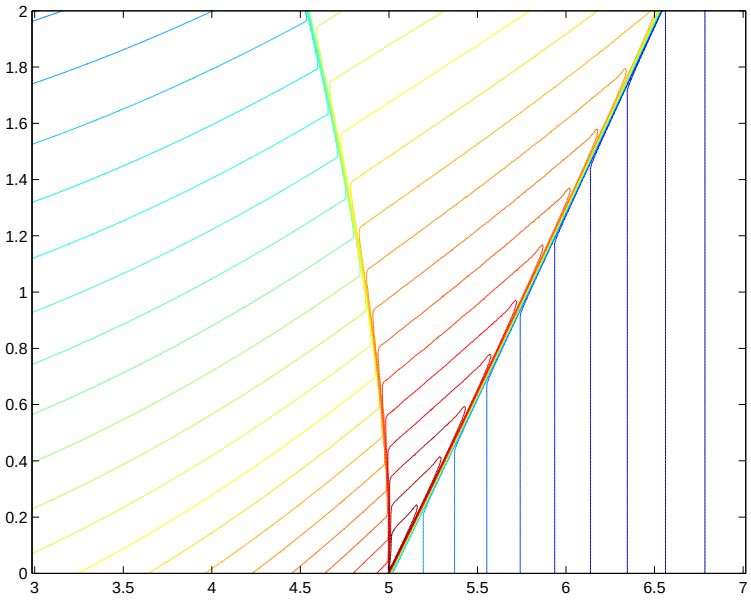

Fig. 4.8. Example 4.5: The contour of the rest energy density logarithm within the spacetime domain $[3, 7] \times [t_0, t_0 + 2]$.

Fig. 4.8 gives the contour of the rest energy density logarithm within the spacetime domain $[3, 7] \times [t_0, t_0 + 2]$. Two relativistic shock waves are initially formed, and the stronger and

straight moves to the right (the TOV region) while the weaker and curved propagates in the FRW-1 region. A expanding pocket of higher density is produced and then interacting with both FRW-1 and TOV metrics.

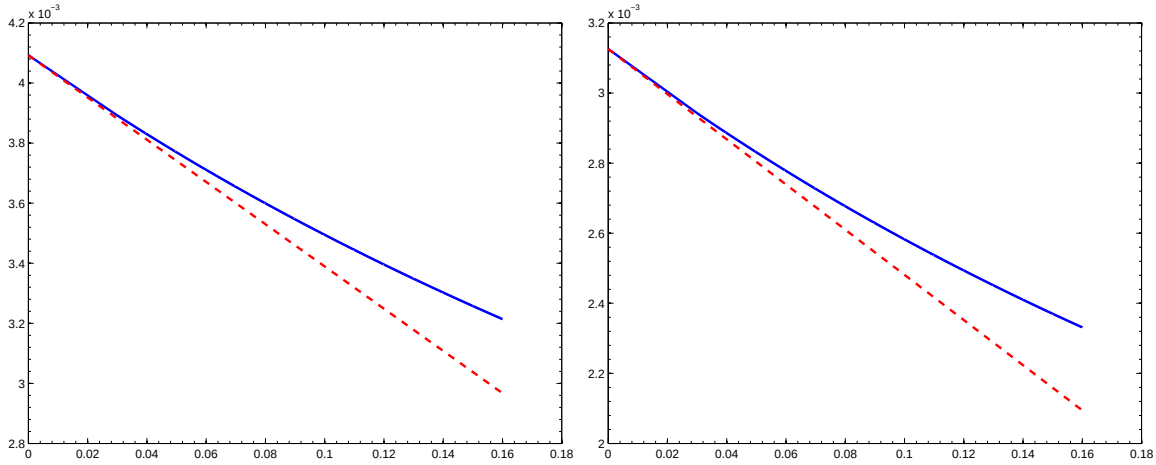


Fig. 4.9. Example 4.5: Comparison of the reference (solid lines) and GRP solver based solutions (dash lines). The left and right are the first and the second components of $\boldsymbol{U}(t_0+\tau, r_0)$, respectively. The horizontal axis is the simulation time $\tau$.

Since this problem itself is GRP, it may be used to validate the accuracy of our GRP solver presented in Section 3.2.3. Fig. 4.9 gives a comparison of the GRP solver based solutions at the interface

$$\boldsymbol{U}^{\mathrm{GRP}}(t_0+\tau, r_0) = \boldsymbol{U}^{\mathrm{RP}} + \left(\frac{\partial \boldsymbol{U}}{\partial t}\right)^{\mathrm{GRP}} \tau,$$

with the reference numerical solutions denoted by $\boldsymbol{U}^{\mathrm{REF}}(t_0+\tau, r_0)$, where $\boldsymbol{U}^{\mathrm{RP}}$ is the exact solution to the (classical) RP (3.7) with $A_* = A(t_0, r_0), B_* = B(t_0, r_0)$, and the initial data $\boldsymbol{U}_L$ and $\boldsymbol{U}_R$ given by the left- and right-side limits at $r = r_0$ of the initial data (4.8), and $(\partial \boldsymbol{U}/\partial t)^{\mathrm{GRP}}$ is computed by resolving the GRP at $r = r_0$. The reference solutions $\boldsymbol{U}^{\mathrm{REF}}(t_0+\tau, r_0)$ are computed by a second-order accurate MUSCL method with the Godunov flux on a very fine uniform mesh with the spatial step-size of $10^{-6}$. Table 4.4 lists the errors approximately evaluated by

$$e_{\mathrm{GRP}}(\tau) = \left\| \boldsymbol{U}^{\mathrm{GRP}}(t_0+\tau, r_0) - \boldsymbol{U}^{\mathrm{REF}}(t_0+\tau, r_0) \right\|_2,$$

and corresponding convergence rates of the GRP solver. The results show that the GRP solver has second-order accuracy with respect to $\tau$ and thus the accuracy of the limiting values $(\partial \boldsymbol{U}/\partial t)^{\mathrm{GRP}}$ is validated.

**Example 4.6 (Time reversal model)** The example considers reversing time and running the matched spacetime given in Example 4.5. For this purpose, the setup of this

Table 4.4
Example 4.5: Numerical errors and corresponding convergence rates of the GRP solver based solution.

| $\tau$ | 0.16 | 0.14 | 0.12 | 0.1 | 0.08 | 0.06 | 0.04 | 0.02 |
|---|---|---|---|---|---|---|---|---|
| $e_{\mathrm{GRP}}(\tau)$ | 3.42e-4 | 2.70e-4 | 2.04e-4 | 1.46e-4 | 9.67e-5 | 5.62e-5 | 2.59e-5 | 6.70e-6 |
| order | – | 1.78 | 1.80 | 1.83 | 1.86 | 1.88 | 1.92 | 1.95 |

problem is the same as that for Example 4.5 except that the sign of the time is changed from positive to negative. In other words, the initial time for this test is $t_0 = -\frac{r_0(1+v_0^2)}{2v_0}$.

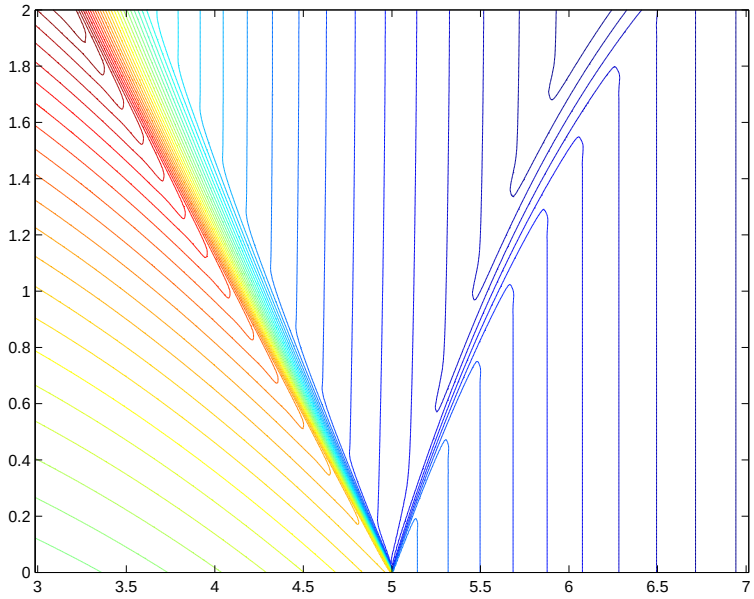

Fig. 4.10. Same as Fig. 4.8, except for Example 4.6.

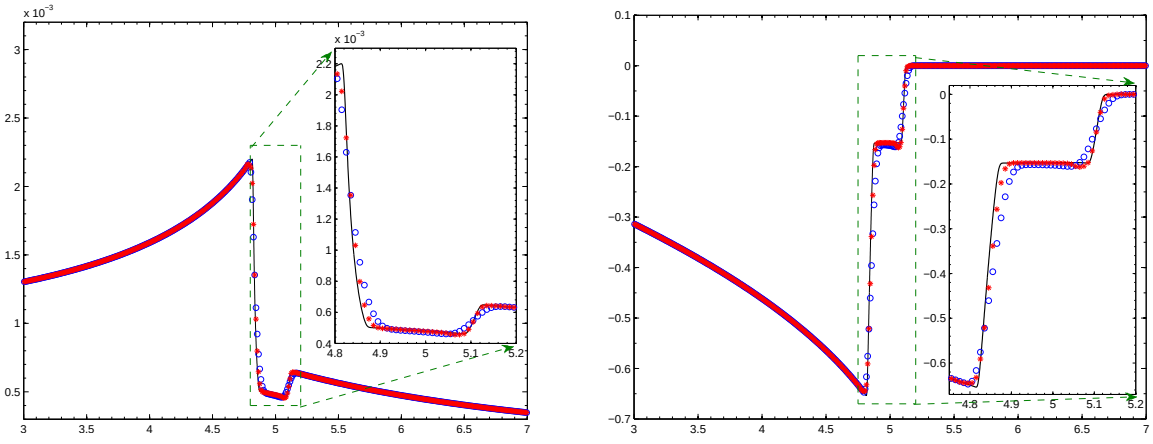

Fig. 4.11. Same as Fig. 4.3, except for Example 4.6.

Fig. 4.10 gives the contour of the rest energy density logarithm within the spacetime domain $[3, 7] \times [t_0, t_0 + 2]$ given by the GRP scheme with 400 uniform cells. From the

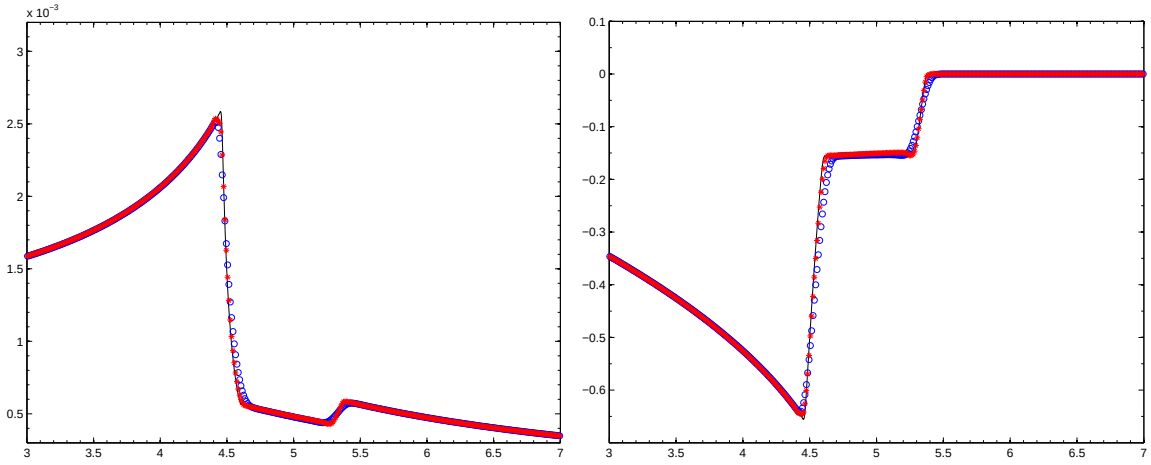


Fig. 4.12. Same as Fig. 4.3, except for Example 4.6 and $t = t_0 + 0.6$.

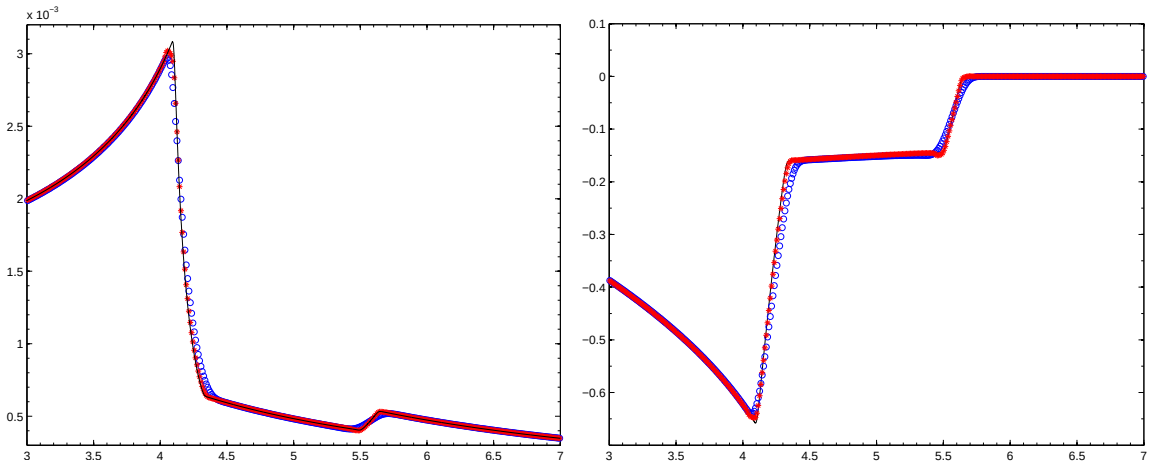


Fig. 4.13. Same as Fig. 4.3, except for Example 4.6 and $t = t_0 + 1$.

initial discontinuity, two relativistic rarefaction waves are formed: a stronger wave moving to the left and connecting the FRW and TOV regions while a weaker propagating in the TOV region. A pocket of lower density is produced between the two rarefaction waves. Those are different from the forward time case in Example 4.5, where two shock waves are surrounding a region of higher density. Figs. 4.3–4.5 show the numerical solutions of the fluid variables at $t = t_0 + 0.2$, $t_0 + 0.6$, and $t_0 + 1$ by using the Godunov and GRP schemes with 400 uniform cells, respectively. We see that the results agree well with the reference solutions and the GRP scheme exhibits better resolution than the Godunov scheme. As the time increases, both the rarefaction waves and the pocket are expanding. At the left of this pocket, there is a density spike, growing and moving in the FRW region, and more matter is falling into the center of the universe as the time increase. If the more long time simulation is done, a black hole will be eventually produced [31].

Figs. 4.14 and 4.15 display the numerical solutions and the corresponding errors in the

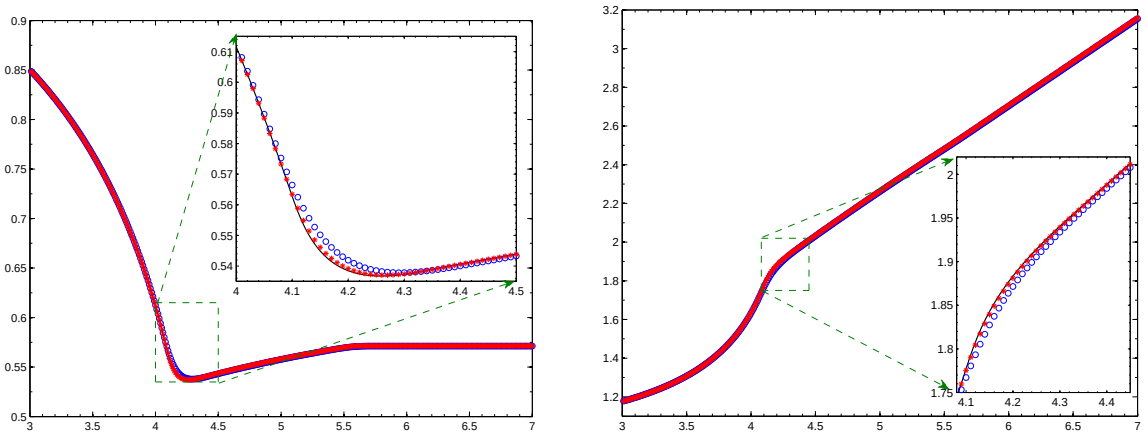

Fig. 4.14. Same as Fig. 4.3, except for Example 4.6 and the metric functions $A$ (left) and $B$ (right) at $t = t_0 + 1$.

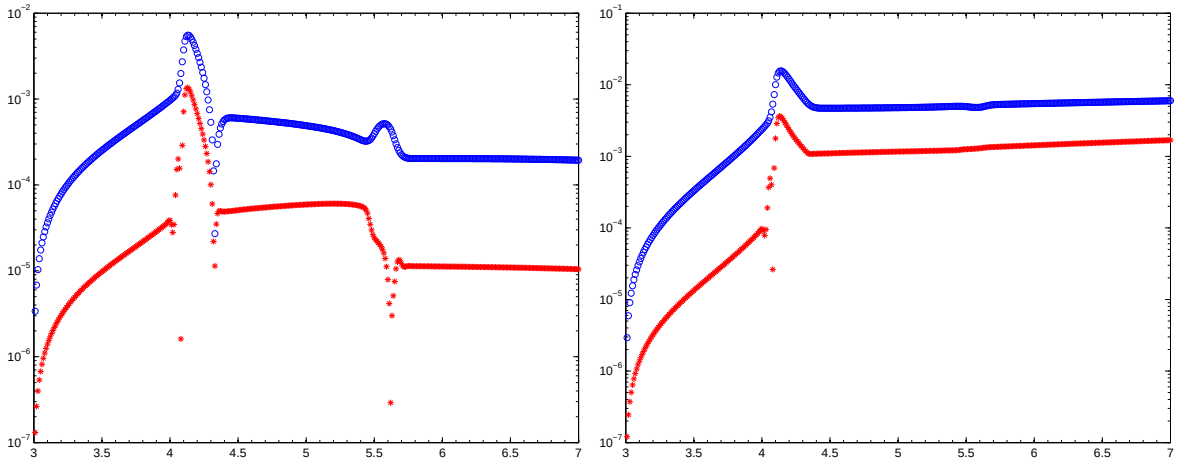

Fig. 4.15. Same as Fig. 4.7, except for Example 4.6.

metric functions $A$ and $B$ at $t = t_0 + 1$ by using the Godunov scheme and the GRP scheme with 400 uniform cells, respectively. These results show that the GRP scheme is much more accurate than the Godunov scheme, and the errors given by the GRP scheme is about ten percent of those computed by the Godunov scheme.

Table 4.5

Example 4.6: Numerical errors and corresponding convergence rates of the GRP solver based solution.

| $\tau$ | 0.16 | 0.14 | 0.12 | 0.1 | 0.08 | 0.06 | 0.04 |
|---|---|---|---|---|---|---|---|
| $e_{\mathrm{GRP}}(\tau)$ | 2.74e-8 | 2.09e-8 | 1.53e-8 | 1.06e-8 | 6.75e-9 | 3.77e-9 | 1.66e-9 |
| order | – | 2.03 | 2.02 | 2.02 | 2.02 | 2.02 | 2.02 |

This reversing time problem is still a GRP. The GRP solver based solutions $\boldsymbol{U}^{\mathrm{GRP}}(t_0+\tau, r_0)$ are plotted in dash lines in Fig. 4.16 in comparison to the reference solutions given by

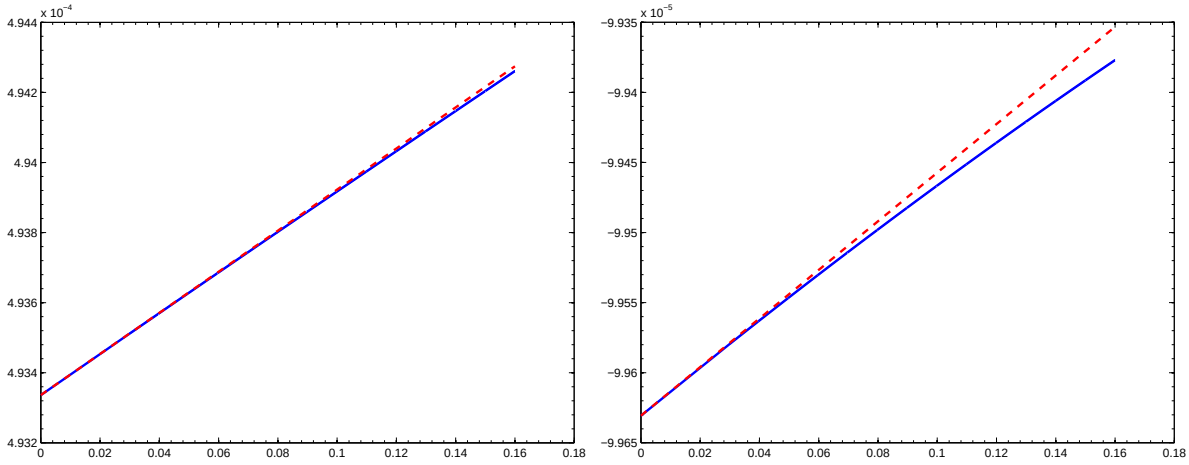


Fig. 4.16. Same as Fig. 4.9, except for Example 4.6.

a second-order accurate MUSCL method with the Godunov flux on a very fine uniform mesh with the spatial step-size of $10^{-6}$. The data in Table 4.5 show that second-order rates of convergence can be obtained for the proposed GRP solver and thus the accuracy of our GRP solver is validated.

## 5 Conclusions

The paper developed a second-order accurate direct Eulerian generalized Riemann problem (GRP) scheme for the spherically symmetric general relativistic hydrodynamical (RHD) equations and a second-order accurate discretization for the spherically symmetric Einstein (SSE) equations. Different from the resulting Godunov-type schemes based on exact or approximate Riemann solvers in general relativistic case, the GRP scheme could not be directly obtained by a local change of coordinates from the special relativistic case. In the GRP scheme, the Riemann invariants and the Runkine-Hugoniot jump conditions were directly used to analytically resolve the left and right nonlinear waves of the local GRP in the Eulerian formulation together with the local change of the metrics to obtain the limiting values of the time derivatives of the conservative variables along the cell interface and the numerical flux for the GRP scheme. Comparing to the GRP schemes for special RHDs [40], the derivation of the present GRP scheme is more technique. The energy-momentum tensor obtained in the GRP solver was utilized to evaluate the fluid variables in the SSE equations and the continuity of the metrics was constrained at the cell interfaces. Several numerical examples were presented to demonstrate the accuracy and effectiveness of the proposed GRP scheme, in comparison with the first-order accurate Godunov scheme.

**Acknowledgements**

This work was partially supported by the National Natural Science Foundation of China (Nos. 91330205 & 11421101).

## Appendix A The Godunov scheme used in Section 4

Assume that the "initial" data at time $t_n$ are

$$\begin{cases} \boldsymbol{U}_h(t_n, r) = \boldsymbol{U}_j^n, \\ \begin{pmatrix} A_h(t_n, r) \\ B_h(t_n, r) \end{pmatrix} = \dfrac{r_{j+\frac{1}{2}} - r}{\Delta r} \begin{pmatrix} A^n_{j-\frac{1}{2}} \\ B^n_{j-\frac{1}{2}} \end{pmatrix} + \dfrac{r - r_{j-\frac{1}{2}}}{\Delta r} \begin{pmatrix} A^n_{j+\frac{1}{2}} \\ B^n_{j+\frac{1}{2}} \end{pmatrix}, \end{cases}$$

for $r \in I_j$, where $A_h(t_n, r)$ and $B_h(t_n, r)$ are continuous at cell interface.

`Step I`. Evolve the solution $\boldsymbol{U}$ at $t = t_{n+1}$ of (2.7) by

$$\begin{aligned} \boldsymbol{U}_j^{n+1} = \boldsymbol{U}_j^n - \frac{\Delta t_n}{\Delta r} \left( \sqrt{A^n_{j+\frac{1}{2}} B^n_{j+\frac{1}{2}}} \boldsymbol{F}\left( \boldsymbol{U}^{\mathrm{RP},n}_{j+\frac{1}{2}} \right) - \sqrt{A^n_{j-\frac{1}{2}} B^n_{j-\frac{1}{2}}} \boldsymbol{F}\left( \boldsymbol{U}^{\mathrm{RP},n}_{j-\frac{1}{2}} \right) \right) \\ + \Delta t_n \boldsymbol{S}\left( r_j, A_j^n, B_j^n, \boldsymbol{U}_j^n \right), \end{aligned}$$

where $A_j^n := \frac{1}{2}\left( A^n_{j-\frac{1}{2}} + A^n_{j+\frac{1}{2}} \right), B_j^n := \frac{1}{2}\left( B^n_{j-\frac{1}{2}} + B^n_{j+\frac{1}{2}} \right)$, and $\boldsymbol{U}^{\mathrm{RP},n}_{j+\frac{1}{2}}$ is the value at $r = r_{j+\frac{1}{2}}$ of the exact solution to the following RP

$$\begin{cases} \dfrac{\partial \boldsymbol{U}}{\partial t} + \sqrt{A^n_{j+\frac{1}{2}} B^n_{j+\frac{1}{2}}} \dfrac{\partial \boldsymbol{F}(\boldsymbol{U})}{\partial r} = 0, \qquad r > 0,\ t > t_n, \\ \boldsymbol{U}(t_n, r) = \begin{cases} \boldsymbol{U}_j^n, & r < r_{j+\frac{1}{2}}, \\ \boldsymbol{U}_{j+1}^n, & r > r_{j+\frac{1}{2}}, \end{cases} \end{cases}$$

`Step II`. Calculate $A^{n+1}_{j+\frac{1}{2}}$ and $B^{n+1}_{j+\frac{1}{2}}$, following `Step V` of the GRP scheme in Section 3.1.

## References

[1] M. Ben-Artzi and J. Falcovitz, A second-order Godunov-type scheme for compressible fluid dynamics, *J. Comput. Phys.*, 55 (1984), 1-32.

[2] M. Ben-Artzi and J. Falcovitz, *Generalized Riemann Problems in Computational Fluid Dynamics*, Cambridge University Press, 2003.

[3] M. Ben-Artzi and J.Q. Li, Hyperbolic balance laws: Riemann invariants and the generalized Riemann problem, *Numer. Math.*, 106 (2007), 369-425.

[4] M. Ben-Artzi, J.Q. Li, and G. Warnecke, A direct Eulerian GRP scheme for compressible fluid flows, *J. Comput. Phys.*, 218 (2006), 19-43.

[5] J.A. Font, Numerical hydrodynamics and magnetohydrodynamics in general relativity, *Living Rev. Relativity*, 11 (2008), 7.

[6] E. Gourgoulhon, Simple equations for general relativistic hydrodynamics in spherical symmetry applied to neutron star collapse, *Astron. Astrophys.*, 252 (1991), 651-663.

[7] J. Groah, J. Smoller, and B.Temple, *Shock wave interactions in general relativity*, Springer Monographs in Mathematics, Springer, New York, 2007.

[8] F.S. Guzmán, F.D. Lora-Clavijo, and M.D. Morales, Revisiting spherically symmetric relativistic hydrodynamics, *Rev. Mex. Fis. E*, 58 (2012), 84-98.

[9] E. Han, J.Q. Li, and H.Z. Tang, An adaptive GRP scheme for compressible fluid flows, *J. Comput. Phys.*, 229 (2010), 1448-1466.

[10] E. Han, J.Q. Li, and H.Z. Tang, Accuracy of the adaptive GRP scheme and the simulation of 2-D Riemann problems for compressible Euler equations, *Commun. Comput. Phys.*, 10 (2011), 577-606.

[11] L.D. Landau and E.M. Lifschitz, *Fluid Meshanics*, Pergaman Press, 1987.

[12] J.Q. Li and G.X. Chen, The generalized Riemann problem method for the shallow water equations with bottom topography, *Int. J. Numer. Meth. in Eng.*, 65 (2006), 834-862.

[13] J.Q. Li, Q.B. Li, and K. Xu, Comparisons of the generalized Riemann solver and the gas-kinetic scheme for inviscid compressible flow simulations, *J. Comput. Phys.*, 230 (2011), 5080-5099.

[14] J.Q. Li, T.G. Liu, and Z.F. Sun, Implementation of the GRP scheme for computing radially symmetric compressible fluid flows, *J. Comput. Phys.*, 228 (2009), 5867-5887.

[15] T. Li and W.C. Yu, *Boundary Value Problem for Quasilinear Hyperbolic Systems*, Mathematics Department, Duke University, 1985.

[16] J.Q. Li and Y.J. Zhang, The adaptive GRP scheme for compressible fluid flows over unstructured meshes, *J. Comput. Phys.*, 242 (2013), 367-386.

[17] M. Liebendöerfer, S. Rosswog, and F.-K. Thielemann, An adaptive grid, implicit code for spherically symmetric, general relativistic hydrodynamics in comoving coordinates, *Astrophys. J. Suppl.*, 141 (2002), 229-246.

[18] M. Liebendörfer, O.E.B. Messer, A. Mezzacappa, S.W. Bruenn, C.Y. Cardall, and F.K. Thielemann, A Finite difference representation of neutrino radiation hydrodynamics for spherically symmetric general relativistic supernova simulations, *Astrophys. J. Suppl.*, 150 (2004), 263-316.

[19] J.M. Martí and E. Müller, Numerical hydrodynamics in special relativity, *Living Rev. Relativity*, 6 (2003), 7.

[20] M.M. May and R.H. White, Hydrodynamic calculations of general relativistic collapse, *Phys. Rev. D*, 141 (1996), 1232-1241.

[21] M.M. May and R.H. White, Stellar dynamics and gravitational collapse, *Methods Comput. Phys.*, 7 (1967), 219-258.

[22] E. O'Connor and C.D. Ott, A new open-source code for spherically symmetric stellar collapse to neutron stars and black holes, *Class. Quantum Grav.*, 27 (2010), 114103.

[23] D.H. Park, I. Cho, G. Kang, and H.M. Lee, A fully general relativistic numerical simulation code for spherically symmetric matter, *J. Korean Phys. Soc.*, 62 (2013), 393-405.

[24] J.A. Pons, J.A. Font, J.M. Ibáñez, J.M. Martí, and J.A. Miralles, General relativistic hydrodynamics with special relativistic Riemann solvers, *Astron. Astrophys.*, 339 (1998), 638-642.

[25] J.Z. Qian, J.Q. Li, and S.H. Wang, The generalized Riemann problems for compressible fluid flows: Towards high order, *J. Comput. Phys.*, 259 (2014), 358-389.

[26] D. Radice and L. Rezzolla, Discontinuous Galerkin methods for general-relativistic hydrodynamics: Formulation and application to spherically symmetric spacetimes, *Phys. Rev. D.*, 84 (2011), 024010.

[27] J.V. Romero, J.M. Ibáñez, J.M. Martí, andJ.A. Miralles, A new spherically symmetric general relativistic hydrodynamical code, *Astrophys. J*, 46 (1996), 839-854.

[28] J. Smoller and B. Temple, Global solutions of the relativistic Euler equations, *Comm. Math. Phys.*, 157 (1993), 67-99.

[29] H.Z. Tang and T. Tang, Adaptive mesh methods for one- and two-dimensional hyperbolic conservation laws, *SIAM J. Numer. Anal.*, 41 (2003), 487-515.

[30] B. Temple and J. Smoller, Expanding wave solutions of the Einstein equations that induce an anomalous acceleration into the Standard Model of Cosmology, *Proc. Natl Acad. Sci.*, 106 (2009), 14213-14218.

[31] Z. Vogler, *The numerical simulation of general relativistic shock waves by a locally inertial Godunov method featuring dynamic time dilation*, Ph.D. thesis, University of California, 2010.

[32] Z. Vogler and B. Temple, Simulation of general relativistic shock wave interactions by a locally inertial Godunov method featuring dynamical time dilation, *Proc. R. Soc. A*, 468 (2012), 1865-1883.

[33] J.R. Wilson, Numerical study of fluid flow in a Kerr space, *Astrophys. J.*, 173 (1972), 431-438.

[34] J.R. Wilson and G.J. Mathews, *Relativistic Numerical Hydrodynamics*, Cambridge University Press, 2003.

[35] K.L. Wu and H.Z. Tang, Finite volume local evolution galerkin method for two-dimensional relativistic hydrodynamics, *J. Comput. Phys.*, 256 (2014), 277-307.

[36] K.L. Wu and H.Z. Tang, High-order accurate physical-constraints-preserving finite difference WENO schemes for special relativistic hydrodynamics, *J. Comput. Phys.*, 298 (2015), 539-564.

[37] K.L. Wu, Z.C. Yang, and H.Z. Tang, A third-order accurate direct Eulerian GRP scheme for the Euler equations in gas dynamics, *J. Comput. Phys.*, 264 (2014), 177-208.

[38] K.L. Wu, Z.C. Yang, and H.Z. Tang, A third-order accurate direct Eulerian GRP scheme for one-dimensional relativistic hydrodynamics, *East Asian J. Appl. Math.*, 4 (2014), 95-131.

[39] S. Yamada, An implicit Lagrangian code for spherically symmetric general relativistic hydrodynamics with an approximate Riemann solver, *Astrophys. J.*, 475 (1997), 720-739.

[40] Z.C. Yang, P. He, and H.Z. Tang, A direct Eulerian GRP scheme for relativistic hydrodynamics: One-dimensional case, *J. Comput. Phys.*, 230 (2011), 7964-7987.

[41] Z.C. Yang and H.Z. Tang, A direct Eulerian GRP scheme for relativistic hydrodynamics: Two-dimensional case, *J. Comput. Phys.*, 231 (2012), 2116-2139.